NASA Contractor Report 145251

CALCULATION OF LATERAL-DIRECTIONAL STABILITY DERIVATIVES FOR WING-BODY COMBINATIONS WITH AND WITHOUT JET-INTERACTION EFFECTS

C. Edward Lan

NASA Grant NSG-1139

THE UNIVERSITY OF KANSAS CENTER FOR RESEARCH, INC.
Lawrence, KS 66045

August 1977

National Aeronautics and
Space Administration

Langley Research Center
Hampton, Virginia 23665

Calculation of Lateral-Directional Stability Derivatives for Wing-Body Combinations with and without Jet-Interaction Effects

by

C. Edward Lan

Technical Report CRINC-FRL-281-1

August 1977

The Flight Research Laboratory
The University of Kansas Center for Research, Inc.
Lawrence, Kansas 66045

Prepared under NASA Grant NSG 1139
for
Langley Research Center
National Aeronautics and Space Administration

Table of Contents

Summary

A theoretical method is presented for predicting the lateral-directional stability derivatives of wing-body combinations with or without the blowing jet effect. The fuselage effect is accounted for by the axial distribution of G.N. Ward's vortex multiplets. Comparison of the predicted results with experiment and other theoretical methods shows good agreement for configurations without the blowing jet. More applicable experimental data with blowing jets are needed to establish the accuracy of the theory.

1. List of Symbols

AR	aspect ratio
b	span
c	chord length
C_{D_i}	induced drag coefficient
C_L	lift coefficient
C_ℓ	rolling moment coefficient
C_m	pitching moment coefficient about y-axis
c_N	sectional normal force coefficient
C_N	total normal force coefficient
C_n	yawing moment coefficient
C_p	pressure coefficient
c_t	tip chord
C_T	thrust coefficient
C_y	side force coefficient
$C_{\ell\beta}$	$= \frac{\partial C_\ell}{\partial \bar{\beta}}$, per radian
C_{n_β}	$= \frac{\partial C_n}{\partial \bar{\beta}}$, per radian
$C_{y\beta}$	$= \frac{\partial C_y}{\partial \bar{\beta}}$, per radian
$C_{\ell p}$	$= \partial C_\ell / \partial (\frac{pb}{2V_\infty})$
C_{np}	$= \partial C_n / \partial (\frac{pb}{2V_\infty})$
C_{yp}	$= \partial C_y / \partial (\frac{pb}{2V_\infty})$
$C_{\ell r}$	$= \partial C_\ell / \partial (\frac{rb}{2V_\infty})$
C_{n_r}	$= \partial C_n / \partial (\frac{rb}{2V_\infty})$
C_{yr}	$= \partial C_y / \partial (\frac{rb}{2V_\infty})$
$C_{t,tip}$	tip suction coefficient

f_n	strength of fuselage flow singularities of n th Fourier mode
G(x)	tip suction singularity parameter
ℓ	fuselage length
M	Mach number, or number of integration stations
N	number of integration points
n	number of Fourier modes of induced velocities matched to satisfy the fuselage boundary condition (excluding the zero-order mode).
N_F	number of fuselage control or integration stations.
$[N^{(n)}]_{ik}$	the induced normal velocity of the n^{th} Fourier mode at the fuselage control station i due to a unit strength of flow singularity at the integration station k.
$[N]_{ik}$	the induced normal velocity at the control point i due to a unit strength of the horseshoe vortex density at k.
p	roll rate, rad./sec.
r	radial coordinate, or yaw rate in rad./sec.
R(x)	fuselage radius
s_t	tip suction per unit length
S_w	reference wing area
$[S^{(n)}]_{ik}$	the induced tangential velocity of the n^{th} Fourier mode at the control point i due to a unit strength of flow singularity at the integration station k.
T	$= \rho_\infty / \rho_j$
u,v,w	nondimensional induced velocity components in the x, y and z directions, respectively.
V	velocity

W	wing section width
x,y,z	rectangular coordinate system with positive x-axis pointing downstream, positive y-axis pointing to the right and positive z-axis pointing upward
x_p	the fuselage station behind which the potential flow ceases to exist and is taken to be $0.378 + 0.527 x'_p/\ell$ from nose.
x'_p	the fuselage station at which the rate of change of the fuselage cross-section area first reaches its maximum negative value.
$z_c(x)$	camber coordinate
α	angle of attack in degrees
β	$=\sqrt{1 - M_\infty}$
$\bar{\beta}$	sideslip angle, radian
γ	vortex density
λ	taper ratio
Λ	sweep angle
Γ	dihedral angle
$\Gamma(x,y)$	accumulated circulation
μ	$= V_\infty/V_j$
μ'	$=\mu\cos\alpha$
ϕ	nondimensional velocity potential
ς	density
$\bar{\theta}$	angle between camber line and chord, including flap angle, if any.

Subscripts

a	antisymmetric
c	chordwise
f	fuselage
ff	fuselage control stations being influenced by fuselage flow singularities
fJ	fuselage control stations being influenced by jet vortices
fw	fuselage control stations being influenced by wing vortices
ℓ	leading edge
j	jet flow
jj	jet flow perturbation due to jet vortices
JJ	jet control points being influenced by jet vortices
JW	jet control points being influenced by wing vortices
Jf	jet control points being influenced by fuselage flow singularities.
oj	external flow perturbation due to jet vortices
r	radial direction in the cylindrical coordinate system
s	spanwise, or symmetric
t	trailing edge, or tail
w	wing
Γ	circulation
θ	circumferential direction in the cylindrical coordinate system
∞	freestream

2. Introduction

It has been shown that upper-surface-blowing (USB) swept-wing configurations have unsatisfactory Dutch roll characteristics without stability augmentation (Ref.1). In an effort to evaluate the jet-interaction effects on the lateral-directional stability derivatives, and hence the lateral-directional dynamic characteristics, the present investigation was initiated.

It is well known that some lateral-directional stability derivatives, in particular the dihedral effect ($C_{\ell\beta}$), depend significantly on the wing-body interaction (Ref. 2, Chapter 4). In addition, the fuselage will contribute to the derivatives $C_{y\beta}$, $C_{n\beta}$, C_{yr}, and C_{nr}. Therefore, the computer program developed earlier without the fuselage effect (Ref. 3) must be revised.

The existing methods for representing the fuselage effect are based on either the image method (See Ref. 4), or the surface singularity distribution (Refs. 4,5,6). The former method is applicable only to long cylindrical bodies with constant radius. On the other hand, the latter method can deal with bodies of arbitrary shape. However, the computer time and the memory requirement would be greatly increased. In order to keep the computer memory requirement to a minimum and yet have the capability of dealing with arbitrary bodies of revolution, a method based on the axial distribution of flow singularities will be developed in Section 3.1. The fuselage effect on the wing-jet interaction will be formulated in Section 3.2. Many ideas used in computing the lateral-directional stability derivatives in subsonic flow have been discussed

in the NACA and NASA literature, mostly based on the lifting-line theory. Some of these ideas will be reformulated for the use in the present lifting-surface theory (Ref. 7) in Section 3.3.

3. Theoretical Formulation

The basic assumption in the formulation is that the linear, potential, subsonic flow theory is applicable. The quasi-vortex-lattice method of Reference 7 is used to formulate the wing and jet boundary conditions (Refs. 8 and 9).

3.1 Fuselage effect without jet interaction

It is assumed that the fuselage is a body of revolution with arbitrary radius distribution. It is not restricted to a slender body. The fuselage camber is not accounted for in the present program, although this restriction can be easily removed.

To represent the fuselage effect, the axial distribution of G.N. Ward's vortex multiplets (Ref. 10) will be used. According to Reference 10, the velocity potential due to the axial distribution of vortex multiplets with strength $f_n(\xi)$ is given by

$$\phi_f(x,\theta,r) = -\frac{1}{4\pi} \sum_n \left\{ \begin{matrix} \cos n\theta \\ \sin n\theta \end{matrix} \right\} \int_{x_{fl}}^{x_{ft}} \frac{\left[x-\xi+\sqrt{(x-\xi)^2+\beta^2 r^2} \right]^n}{r^n \sqrt{(x-\xi)^2+\beta^2 r^2}} f_n(\xi) d\xi \tag{1}$$

where cos n θ is to be used for the symmetrical cases and sin n θ for the antisymmetrical cases, such as in computing the lateral-directional stability derivatives. The coordinate system for Eq. (1) is indicated in Figure 1. Note that if n=o in Eq. (1), the resulting

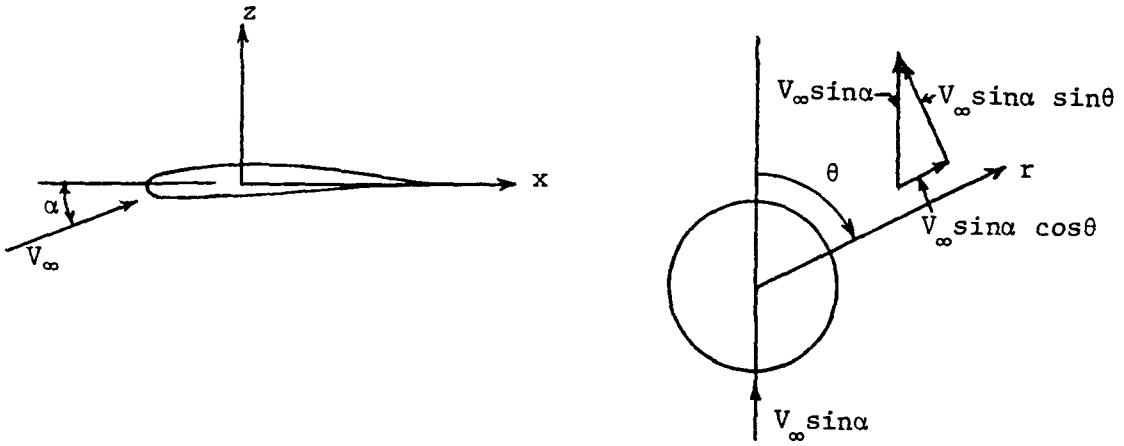

Figure 1. Fuselage Cylindrical Coordinate System

velocity potential is for the familiar line source distribution. Before Eq. (1) is differentiated to obtain the velocity components, it is advantageous to integrate the integral by parts to obtain

$$\phi_f(x,\theta,r) = -\frac{1}{4\pi}\sum_n \begin{Bmatrix} \cos n\theta \\ \sin n\theta \end{Bmatrix} \left\{ f_n(\xi) F_n(x,r,\xi) \Big|_{x_{f\ell}}^{x_{ft}} - \int_{x_{f\ell}}^{x_{ft}} F_n(x,r,\xi) f_n'(\xi) d\xi \right\} \tag{2}$$

where

$$F_n(x,r,\xi) = \int \frac{\left[x-\xi+\sqrt{(x-\xi)^2+\beta^2 r^2}\right]^n}{r^n \sqrt{(x-\xi)^2+\beta^2 r^2}} d\xi$$

$$= \begin{cases} -\ln \dfrac{x-\xi+\sqrt{(x-\xi)^2+\beta^2 r^2}}{\beta r}, & n=0 \\ -\dfrac{1}{n}\dfrac{\left[x-\xi+\sqrt{(x-\xi)^2+\beta^2 r^2}\right]^n}{r^n}, & n\neq 0 \end{cases} \tag{3}$$

The boundary conditions in symmetrical flow can be written as follows:

On the wing surface:

$$\frac{\partial \phi_w}{\partial z} + \frac{\partial \phi_f}{\partial z} = \frac{\partial z_c}{\partial x} - \sin\alpha \tag{4}$$

On the fuselage surface: (see Ref. 11, Chapter 9)

$$\frac{\partial \phi_f}{\partial r} + \frac{\partial \phi_w}{\partial r} = \cos\alpha \frac{dR}{dx} - \sin\alpha \cos\theta \tag{5}$$

Note that both ϕ_w and ϕ_f in Eqs. (4) and (5) are nondimensionalized with respect to V_∞. In Eq. (5), $\frac{\partial \phi_f}{\partial r}$ is needed. It is obtained from Eq. (2) by differentiation to give

$$\frac{\partial \phi_f}{\partial r} = -\frac{1}{4\pi} \sum_n \cos n\theta \left\{ f_n(x_{ft}) \frac{\partial F_n}{\partial r}(x_{ft}) - f_n(x_{fl}) \frac{\partial F_n}{\partial r}(x_{fl}) - \int_{x_{fl}}^{x_{ft}} \frac{\partial F_n}{\partial r}(x, r, \xi) f_n'(\xi) d\xi \right\} \tag{6}$$

Eq. (6) can be simplified as follows. By the following transformation,

$$\xi = x_{fl} + \frac{x_{ft} - x_{fl}}{2}(1 - \cos\theta_1) \tag{7}$$

the integral becomes

$$\int_{x_{fl}}^{x_{ft}} \frac{\partial F_n}{\partial r}(x, r, \xi) f_n'(\xi) d\xi = \frac{x_{ft} - x_{fl}}{2} \int_0^{\pi} \frac{\partial F_n}{\partial r} f_n'(\xi) \sin\theta_1 d\theta_1 \approx \frac{x_{ft} - x_{fl}}{2} \frac{\pi}{N_F} \sum_{k=1}^{N_F} \frac{\partial F_{nk}}{\partial r} f_{nk}' \sin\theta_{1k} \tag{8}$$

where

$$\frac{\partial F_n}{\partial r}(x, r, \xi) = \frac{x - \xi}{r} \frac{\left[x - \xi + \sqrt{(x-\xi)^2 + \beta^2 r^2}\right]^n}{r^n \sqrt{(x-\xi)^2 + \beta^2 r^2}}, \quad n \geq 0 \tag{9}$$

$$\frac{\partial F_n}{\partial r}(x_{ft}) = \frac{\partial F_n}{\partial r}(x, r, x_{ft}) \tag{10}$$

$$\frac{\partial F_{nk}}{\partial r} = \frac{\partial F_n}{\partial r}(x, r, \xi_k) \tag{11}$$

$$\xi_k = x_{fl} + \frac{x_{ft} - x_{fl}}{2}(1 - \cos\theta_{1k}), \quad \theta_{1k} = \frac{2k-1}{2N_F}\pi, \quad k=1,\cdots,N_F \tag{12}$$

and the integral was reduced to a finite sum through the midpoint trapezoidal rule. $f_n(x_{ft})$ in Eq. (6) can be expressed in terms of $f_n'(\xi)$ as follows.

$$f_n(x_{ft}) = f_n(x_{fl}) + \int_{x_{fl}}^{x_{ft}} f_n'(\xi)\,d\xi$$

$$\cong f_n(x_{fl}) + \frac{x_{ft} - x_{fl}}{2}\frac{\pi}{N_F}\sum_{1}^{N_F} f_{nk}' \sin\theta_{1k} \tag{13}$$

It follows that Eq. (6) becomes

$$\frac{\partial\phi_f}{\partial r} = -\frac{1}{4\pi}\sum_n \cos n\theta \left\{ \left[\frac{\partial F_n}{\partial r}(x_{ft}) - \frac{\partial F_n}{\partial r}(x_{fl})\right] f_n(x_{fl}) \right.$$

$$\left. + \frac{x_{ft} - x_{fl}}{2}\frac{\pi}{N_F}\sum_k f_{nk}' \sin\theta_{1k}\left[\frac{\partial F_n}{\partial r}(x_{ft}) - \frac{\partial F_{nk}}{\partial r}\right] \right\} \tag{14}$$

The fuselage surface boundary condition, Eq. (5), will be satisfied at N_F control stations specified in a similar way as in selecting the wing control points (Ref.7):

$$x_{fi} = x_{fl} + \frac{x_{ft} - x_{fl}}{2}(1 - \cos\theta_{1i}), \quad \theta_{1i} = \frac{i\pi}{N_F}, \quad i=1,\cdots,N_F \tag{15}$$

Note that $\frac{\partial\phi_f}{\partial r}$ is expressed in a Fourier cosine series. The wing induced normal velocity, $\frac{\partial\phi_w}{\partial r}$, will also be Fourier-analyzed. Let $[N_{ff}^{(n)}]$ be a matrix with elements being the induced normal velocity of the n^{th} Fourier mode at control station i due to a unit f'_{nk}. Similar definition can also be applied to the matrix $[N_{fw}^{(n)}]$ due to

the wing effect. The detailed expressions are described in Appendix A. After Eq. (14) and the Fourier-analyzed $\frac{\partial \phi_w}{\partial r}$ are substituted into the fuselage boundary condition Eq. (5), and equating each Fourier mode, the following system of equations can be obtained:

$$[R\, N_{ff}^{(0)}]\{f_0'\} = \left\{R\frac{dR}{dx}\cos\alpha - R\,G_0\right\} \tag{16}$$

$$[R^2 N_{ff}^{(1)}]\{f_1'\} + [R^2 N_{fw}^{(1)}]\{\gamma_w\} = \{-R^2\sin\alpha - R^2 G_1\} \tag{17}$$

$$[R^3 N_{ff}^{(2)}]\{f_2'\} + [R^3 N_{fw}^{(2)}]\{\gamma_w\} = \{-R^3 G_2\} \tag{18}$$

etc.

In the above equations, all equations have been multiplied through by R^{n+1}, where R(x) is the fuselage radius. This is numerically expedient in view of the fact that $\partial F_n/\partial r$, which appears in $[N_{ff}^{(n)}]$, contains r^{n+1} in the denominator. G_n in the above equations comes from the first term in Eq. (14), and is defined as

$$G_n = -\frac{1}{4\pi}\left[\frac{\partial F_n}{\partial r}(x_{f_t}) - \frac{\partial F_n}{\partial r}(x_{f_\ell})\right] f_n(x_{f_\ell}) \tag{19}$$

Note that in each of the equations (16)-(18), there are N_F equations because of N_F control stations, but involving (N_F+1) unknowns, f_{n_k}' with k=1, ..., N_F and $f_n(x_{f\ell})$. However, $f_n(x_{f\ell})$ can be obtained directly by evaluating Eqs. (16)-(18) at $x=x_{f\ell}$, i.e., the fuselage nose. The results can be shown to be (see Appendix B)

$$f_0(x_{f_\ell}) = \frac{4\pi R\frac{dR}{dx}\Big|_{x=x_{f\ell}}}{1+g_1} \tag{20}$$

$$f_1(x_{f_\ell}) = -\frac{g\pi}{1+g_1} R\frac{dR}{dx}\Big|_{x=x_{f\ell}} - \left\{\sin\alpha + \sum_m N_{fw_m}^{(1)}\gamma_{w_m}\Big|_{x=x_{f\ell}}\right\} \tag{21}$$

$$f_n(x_{fl}) = 0 \quad , \quad n \geq 2 \tag{22}$$

where

$$g_1 = \frac{1}{\sqrt{1+\beta^2\left(\frac{dR}{dx}\right)^2}}\Bigg|_{x=x_{fl}} \tag{23}$$

Note that in applications, it is not necessary to compute g_1 because if $R\frac{dR}{dx}\Big|_{x=x_{fl}} = 0$, it implies $\frac{dR}{dx}(x_{fl})$ is finite so that g_1 is nonzero. However, $f_n(x_{fl})=0$ whatever g_1 is. On the other hand, if $R\frac{dR}{dx}(x_{fl})$ is finite, this implies $\frac{dR}{dx}(x_{fl}) \to \infty$ if $R(x_{fl}) = 0$, and hence $g_1 = 0$. Eq. (16) can be solved independently of other equations.

The wing surface boundary condition, Eq. (4), can be written in terms of the influence coefficient matrices, $[N_{ww}]$, $[N_{wf}^{(1)}]$, $[N_{wf}^{(2)}]$, etc. as follows:

$$[N_{ww}]\{\gamma_w\} + [N_{wf}^{(1)}]\{f_1'\} + [N_{wf}^{(2)}]\{f_2'\} + \cdots$$
$$= \left\{\frac{\partial z_c}{\partial x} - \sin\alpha - H_1 - [N_{wf}^{(0)}]\{f_0'\}\right\} \tag{24}$$

where H_1 is the contribution of $f_1(x_{fl})$ and its detail expression can be found in Appendix A. Eqs. (17), (18), and (24) can be written in the format of an augmented matrix for solution. Assuming n=2, it follows that

$$\begin{bmatrix} [N_{ww}] & [N_{wf}^{(1)}] & [N_{wf}^{(2)}] \\ [R^2 N_{fw}^{(1)}] & [R^2 N_{ff}^{(1)}] & [0] \\ [R^3 N_{fw}^{(2)}] & [0] & [R^3 N_{ff}^{(2)}] \end{bmatrix} \begin{Bmatrix} \gamma_w \\ f_1' \\ f_2' \end{Bmatrix} = \begin{Bmatrix} \frac{\partial z_c}{\partial x} - \sin\alpha - H_1 - [N_{wf}^{(0)}]\{f_0'\} \\ -R^2\sin\alpha - R^2 G_1 \\ 0 \end{Bmatrix} \tag{25}$$

(Sym)

Note that in Eq. (25), G_i contains γ_w through Eqs. (19) and (21). That particular term should be combined with the appropriate term on the left hand side before the solution is attempted. In all configurations tested so far, the contribution of G_1 to the final solution of γ_w has been found to be relatively small.

For the antisymmetrical case due to sideslipping, steady rolling and steady yawing, the boundary condition can be formulated in a similar manner. Consider the wing boundary condition first. Referring to Fig. (2), the induced normal velocity, which must be produced to cancel the upwash due to dihedral in a sideslip, is given by

$$\frac{\partial \phi}{\partial z} = -\bar{\beta} \sin \Gamma \tag{26}$$

where it is assumed that the wing boundary condition is to be satisfied on the mean surface only and Γ, the dihedral angle, is small enough so that the normal unit vector to the wing surface is essentially in the z-direction. In steady yawing, the sidewash produced on the wing surface would vary

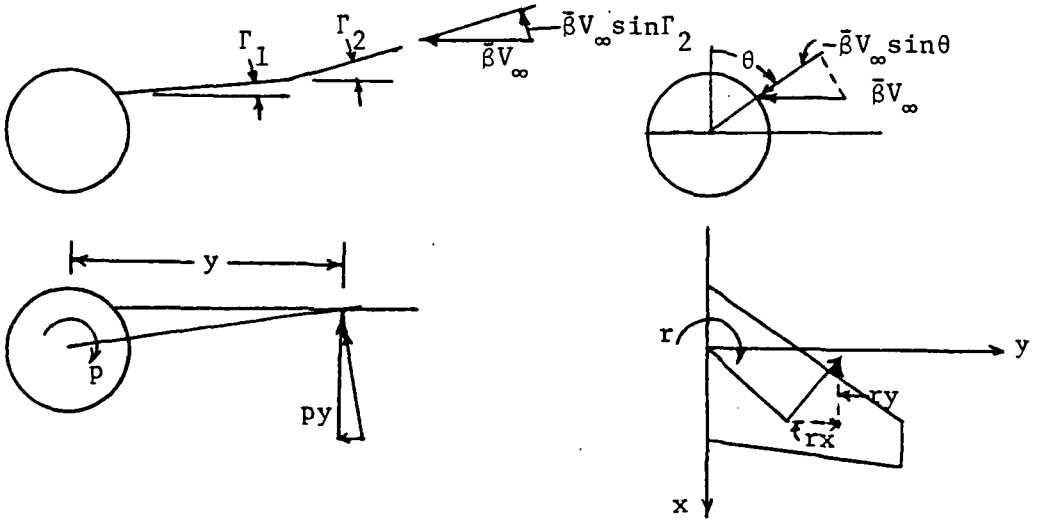

Figure 2 Normal Velocity Components on Wing-Body Surface due to Lateral-Directional modes of motion

from location to location and is given by $r\bar{x}$ as shown in Fig.2. Therefore, it can be considered as in a "variable sideslip" situation with the following boundary condition to be satisfied:

$$\frac{\partial\phi}{\partial z} = -\left(-\frac{r\bar{x}}{V_\infty}\right)\sin\Gamma = \left(\frac{rb}{2V_\infty}\right)\left(\frac{2\bar{x}}{b}\right)\sin\Gamma \tag{27}$$

Similarly, the upwash on the right wing in a positive steady roll is given by py. Hence, the wing boundary condition is

$$\frac{\partial\phi}{\partial z} = -\frac{py}{V_\infty} = -\left(\frac{pb}{2V_\infty}\right)\frac{2y}{b} \tag{28}$$

On the fuselage surface, the sideslip boundary condition is given by (see Fig. 2)

$$\frac{\partial\phi}{\partial r} = -\left(-\bar{\beta}\sin\theta\right) \tag{29}$$

Similarly, in steady yawing, the expression would be

$$\frac{\partial\phi}{\partial r} = -\left(\frac{rb}{2V_\infty}\right)\frac{2\bar{x}}{b}\sin\theta \tag{30}$$

On the other hand, in steady rolling, no normal velocity will be generated by p-motion. Hence,

$$\frac{\partial\phi}{\partial r} = 0 \tag{31}$$

In the case of antisymmetrical flow, the cos n θ in Eq. (14) is to be replaced by sin n θ and the wing-induced velocity on the fuselage surface will be developed in a Fourier sine series. The augmented matrix in this case can be written as, again for n=2,

$$\begin{bmatrix} [N_{ww}] & [N_{wf}^{(1)}] & [N_{wf}^{(2)}] \\ [R^2 N_{fw}^{(1)}] & [R^2 N_{ff}^{(1)}] & [0] \\ [R^3 N_{fw}^{(2)}] & [0] & [R^3 N_{ff}^{(2)}] \end{bmatrix} \begin{Bmatrix} \gamma_w \\ f_1' \\ f_2' \end{Bmatrix} = \begin{Bmatrix} -\bar{\beta}\sin\Gamma + \left(\frac{rb}{2V_\infty}\right)\left(\frac{2\bar{x}}{b}\right)\sin\Gamma \\ -\left(\frac{pb}{2V_\infty}\right)\left(\frac{2y}{b}\right) \\ R^2\bar{\beta} - R^2\left(\frac{rb}{2V_\infty}\right)\left(\frac{2\bar{x}}{b}\right) \\ 0 \end{Bmatrix} \tag{32}$$

where the corresponding G_n for this case are all assumed zero for simplicity. For $\bar{\beta}$ -derivatives, both p and r are assumed zero in

Eq. (32) and β is set to 5°. For p- or r- derivatives, either $\frac{pb}{2V_\infty}$ or $\frac{rb}{2V_\infty}$ is set to 1 and other flow parameters are set to zero.

3.2 Fuselage effect with Jet Interaction

In the wing-jet interaction theory described in Refs. 8 and 12, the solution is obtained by solving the jet-off case first and then the additional effect due to jet interaction. The same concept applies here. The jet-off case has been described in Section 3.1. The jet effect of the symmetrical case is obtained by solving the following system of equations (Ref. 12) for n=2:

Pressure continuity on jet surface

$$[S_{JJ}]_{(j)}\{\gamma_{jj}\} - T(\mu')^2[S_{JJ}]_{(o)}\{\gamma_{oj}\} - T(\mu')^2[S_{Jw}]_{(o)}\{\gamma_{wa}\} - T(\mu')^2[S_{Jf}^{(1)}]\{f_1'\}$$
$$- T(\mu')^2[S_{Jf}^{(2)}]\{f_2'\} = \left\{T(\mu')^2 D_1 - \frac{\partial \phi_j}{\partial s}(M_j) + T(\mu')^2 \frac{\partial \phi_o}{\partial s}(M_o)\right\} \quad (33)$$

Flow tangency on jet surface

$$-[N_{JJ}]_{(j)}\{\gamma_{jj}\} + [N_{JJ}]_{(o)}\{\gamma_{oj}\} + [N_{Jw}]_{(o)}\{\gamma_{wa}\} + [N_{Jf}^{(1)}]\{f_1'\} + [N_{Jf}^{(2)}]\{f_2'\}$$
$$= \left\{-\frac{\vec{V}_\infty \cdot \hat{n}}{\vec{V}_\infty \cdot \vec{e}}(1-\mu') + \frac{\partial \phi_j}{\partial n}(M_j) - \frac{\partial \phi_o}{\partial n}(M_o) - P_1\right\} \quad (34)$$

Flow tangency on wing surface

$$[N_{wJ}]_{(o)}\{\gamma_{oj}\} + [N_{ww}]\{\gamma_{wa}\} + [N_{wf}^{(1)}]\{f_1'\} + [N_{wf}^{(2)}]\{f_2'\} = \{-H_1\} \quad (35)$$

Flow tangency on fuselage-first Fourier mode matching

$$[R^2 N_{fJ}^{(1)}]_{(o)}\{\gamma_{oj}\} + [R^2 N_{fw}^{(1)}]\{\gamma_{wa}\} + [R^2 N_{ff}^{(1)}]\{f_1'\} = \{-R^2 G_1\} \quad (36)$$

Flow tangency on fuselage-second Fourier mode matching

$$[R^3 N_{fJ}^{(2)}]_{(o)}\{\gamma_{oj}\} + [R^3 N_{fw}^{(2)}]\{\gamma_{wa}\} + [R^3 N_{ff}^{(2)}]\{f_2'\} = \{0\} \quad (37)$$

The velocity potential ϕ in Eqs. (33) and (34) is for the wing-body combinations without the jet effect. D_1 in Eq. (33) and P_1 in Eq.(34) are the contribution from $f_1(x_{f\ell})$ and the detail expressions can be found

in Appendix A.

In antisymmetrical case, Eq. (33) remains unchanged in form, except that all influence coefficient matrices must account for antisymmetry and ϕ is interpreted as the antisymmetrical velocity potential for the wing-body combination without the jet effect. Furthermore, the right hand side of Eqs. (35) and (36) will be replaced by zero and that of Eq. (34) by the following expression:

RHS of Eq. (34) for antisymmetrical case $= -\left\{-\bar{\beta}\cos\theta_J + \right.$

$$\left. + \left(\frac{pb}{2V_\infty}\right)\left(\frac{2y}{b}\right)\sin\theta_J + \left(\frac{rb}{2V_\infty}\right)\left(\frac{2x}{b}\right)\cos\theta_J \right\}(1-\mu') \qquad (38)$$

where θ_J is defined in Fig. 3 and the effect of Mach number non-uniformity has been neglected.

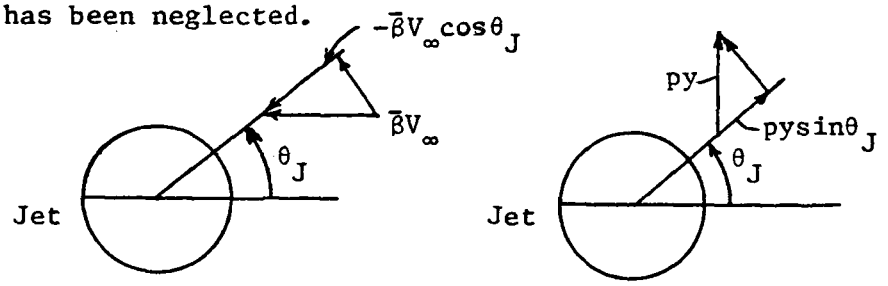

Figure 3 Jet Surface Boundary Condition in Lateral Mode of Motion

3.3 Forces and Moments

3.3.1 Symmetrical aerodynamic characteristics

Once the vortex density distribution on the wing is obtained, the wing aerodynamic characteristics can be calculated by integration. The procedure has been reported earlier (Ref. 8) and therefore, will not be repeated here. The only difference is that the computed vortex density is referred to V_∞ here, instead of $V_\infty \cos\alpha$ in Ref. 8.

The pressure distribution on a body of revolution may be computed

by the following formula (Ref. 11).

$$C_{p(f)} = -2u - [(1-M_\infty^2)u^2 + v^2 + w^2] \tag{39}$$

where u, v, and w are nondimensional perturbed velocity components referred to the freestream velocity. In the fuselage cylindrical coordinate system,

$$v^2 + w^2 = v_\theta^2 + v_r^2 \tag{40}$$

where, referring to Fig. 1,

$$v_\theta = \frac{1}{r}\frac{\partial \phi}{\partial \theta} - \sin\alpha \sin\theta \tag{41}$$

$$v_r = \frac{\partial \phi}{\partial r} + \sin\alpha \cos\theta = \cos\alpha \frac{dR}{dx} \tag{42}$$

with the first term coming from the combined effect of the fuselage and the wing. The last relation in Eq. (42) was obtained from the boundary condition, Eq. (5). Therefore, Eq. (39) can be written as

$$C_{p(f)} = 1 - (1+u)^2 + \left(\cos\alpha \frac{dR}{dx}\right)^2 + \left(\frac{1}{r}\frac{\partial \phi}{\partial \theta} - \sin\alpha \sin\theta\right)^2 \tag{43}$$

The velocity component u due to the fuselage itself is formulated in Appendix C. Once the pressure distribution $C_{p(f)}$ is obtained, the fuselage sectional normal force coefficient referring to the radius can be calculated by integration along the circumference (see Fig. 4):

$$C_{N(f)} = -\frac{1}{r}\int_0^{2\pi} C_{p(f)}(r\,d\theta)\cos\theta = -2\int_0^{\pi} C_{p(f)}\cos\theta\, d\theta \cong -2\frac{\pi}{N_\theta}\sum_k C_{p(f)k}\cos\theta_k \tag{44}$$

One alternative in making the approximate integration in Eq. (44) is to divide (o,π) into two arcs and integrate the results seperately:

$$C_{N(f)} = -2\left\{\int_0^{\theta_1} C_{p(f)}\cos\theta\, d\theta + \int_{\theta_1}^{\pi} C_{p(f)}\cos\theta\, d\theta\right\} \cong -2\left\{\frac{\theta_1}{N_{\theta_1}}\sum_k C_{p(f)k}\cos\theta_k + \frac{\pi-\theta_1}{N_{\theta_2}}\sum_k C_{p(f)k}\cos\theta_k\right\} \tag{45}$$

Eq. (45) is useful if the wing is at any arbitrary location on the fuselage. The wing-fuselage junction will be the dividing point.

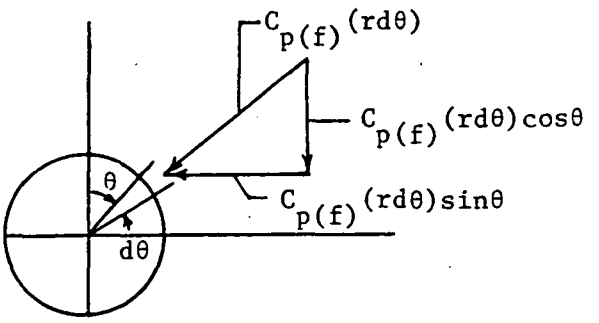

Figure 4 Decomposition of Pressure Force on the Fuselage

With the sectional normal force coefficient calculated, the total normal force coefficient is given by

$$C_{N(f)} = \frac{1}{S_w}\int_{x_{fl}}^{x_p} r c_{N(f)}\, dx \tag{46}$$

where x_p is the fuselage station behind which the potential flow does not exist, and is related to the fuselage station x'_p at which the rate of change of the fuselage cross-section area first reaches its maximum negative value (Ref. 13, also List of Symbols). To integrate Eq. (46) numerically, it is first transformed to an angular integration:

$$x = x_{fl} + \frac{x_{ft} - x_{fl}}{2}(1 - \cos\phi) \tag{47}$$

$$C_{N(f)} = \frac{x_{ft} - x_{fl}}{2\, S_w}\int_0^{\phi_p} r c_{N(f)} \sin\phi\, d\phi \tag{48}$$

With $(x_{fl}-x_{ft}) r c_{N(f)}\ (\sin\phi)/2$ expressed in Fourier cosine series, Eq. (48) can be exactly integrated. This is developed in detail in Appendix C. Similarly, the moment coefficient can be obtained from

$$C_{m(f)} = -\frac{x_{ft} - x_{fl}}{2\, S_w \bar{c}}\int_0^{\phi_p} r c_{N(f)}\, x \sin\phi\, d\phi \tag{49}$$

The relation between x_p and the fuselage geometry has been discussed in Ref. 13 and an empirical formula has been given. The same method is used in the U. S. Air Force Datcom. It should be noted that Eqs. (48) and (49) do not include the second order effect in the angle of attack, or any vortex lift effect.

As shown in Ref. 11, the first harmonics in the last term of Eq. (43) will not contribute to the lift. Since the higher harmonics in $\frac{\partial\phi}{\partial\theta}$ should be small in magnitude, they are ignored in computing the lift and moment in the present computer program.

3.3.2 Lateral-Directional Stability Derivatives

The theoretical prediction of lateral-directional stability derivatives has been discussed previously by Queijo (Ref. 14) with Weissinger's lifting-line formulation. More recently, Hancock and Garner have discussed in detail the mathematical theory and applications for computing the second-order forces and moments with the lifting-surface theory of the kernel function type (Ref. 15). The vortex-lattice method (Refs. 5,16, 17) and the pressure panel method (Ref. 6) can also be used for this purpose. In the present method, the quasi-vortex-lattice method (QVLM) of Ref. 7 will be used to predict the edge forces. It is assumed that the spanwise vortex density γ_y has been predicted in accordance with the QVLM.

(a) Streamwise vortex density distribution γ_x

The basis of the present method is the calculation of the streamwise vortex density (γ_x) distribution on the wing. According to the conservation of vorticity,

$$\frac{\partial \gamma_x}{\partial x} + \frac{\partial \gamma_y}{\partial y} = 0 \tag{50}$$

By integration,

$$\gamma_x = -\int_{x_\ell(y)}^{x} \frac{\partial \gamma_y}{\partial y}\, dx' + \lim_{x \to x_\ell(y)} \gamma_y(x, y) \frac{\partial x_\ell}{\partial y} \tag{51}$$

$$= -\frac{\partial}{\partial y} \int_{x_\ell(y)}^{x} \gamma_y\, dx' \tag{52}$$

If Eq. (50) is regarded as a first order differential equation for γ_x, then the second term on the right hand side of Eq. (51) is the

initial condition obtained from the fact that at the leading edge, the vorticity vector should be parallel to the leading edge. Let

$$\Gamma(x,y) = -\int_{x_l(y)}^{x} \gamma_y(x',y)\,dx' \tag{53}$$

It follows that

$$\gamma_x = \frac{\partial}{\partial y}\Gamma(x,y) \tag{54}$$

The problem of determining γ_x consists of two steps: Firstly, using the predicted γ_y-values at the vortex locations, calculate $\Gamma(x,y)$ values at the same locations. Secondly, differentiate $\Gamma(x,y)$ numerically to find γ_x. It should be remembered that γ_y-values are defined at only a finite number of locations in the chordwise direction. To use these finite number of values in the integral Eq. (53), it is best to develop $\gamma_y \sin\theta$ in a cosine Fourier series, where θ is the angular coordinate in the chordwise coordinate transformation used in the QVLM:

$$x = x_l + \frac{c(y)}{2}(1-\cos\theta) \tag{55}$$

Let

$$f(\theta) = \gamma_y \sin\theta = a_0 + \sum_1^N a_j \cos j\theta \tag{56}$$

The Fourier coefficients can be computed as

$$a_0 = \frac{1}{\pi}\int_0^{\pi} f(\theta)\,d\theta \cong \frac{1}{N}\sum_1^N f(\theta_k) \tag{57}$$

$$a_j = \frac{2}{\pi}\int_0^{\pi} f(\theta)\cos j\theta\,d\theta \cong \frac{2}{N}\sum_1^N f(\theta_k)\cos j\theta_k\,, \quad j \geq 1 \tag{58}$$

$$\theta_k = \frac{2k-1}{2N}\pi \tag{59}$$

Using Eqs. (55) and (56), Eq. (53) becomes

$$\Gamma(x_k, y_k) = -\frac{c(y_k)}{2}\int_0^{\theta_k} \gamma_y \sin\theta\, d\theta = -\frac{c(y_k)}{2}\left[a_0\theta_k + \sum_1^N a_j \frac{\sin j\theta_k}{j}\right] \qquad (60)$$

Eq. (60) has been found to converge very well with respect to N, the number of γ_y-values defined in the chordwise direction.

With discrete values of $\Gamma(x_k,y_k)$ defined over the planform, theoretically it is possible to pass an interpolation surface through these "points", with (x_k,y_k,Γ_k) defining a point in the three-dimensional space. At each point, a tangent plane to the interpolation surface exists. This tangent plane can be constructed if the slopes in two directions (to be specified) at a point are known. These two directions can be conveniently chosen to be x- and y'-axes (see Fig. 5), where

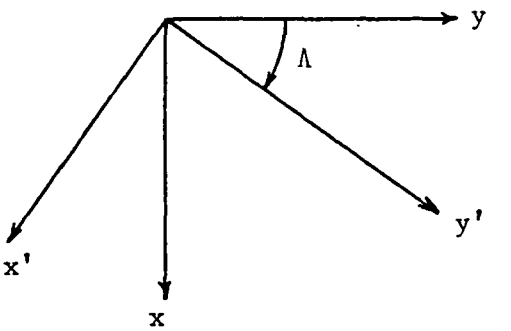

Figure 5 Coordinate Transformation

the y'-axis is along the straight line on which the predicted γ_y-values are situated. It follows that

$$x' = x\cos\Lambda - y\sin\Lambda \qquad (61a)$$

$$y' = x\sin\Lambda + y\cos\Lambda \qquad (61b)$$

$$x = x'\cos\Lambda + y'\sin\Lambda \qquad (62a)$$

$$y = -x'\sin\Lambda + y'\cos\Lambda \qquad (62b)$$

where Λ is the sweep angle of the y'-axis. Therefore,

$$\frac{\partial \Gamma}{\partial y} = \frac{\partial \Gamma}{\partial x'}\frac{\partial x'}{\partial y} + \frac{\partial \Gamma}{\partial y'}\frac{\partial y'}{\partial y} = -\sin\Lambda \frac{\partial \Gamma}{\partial x'} + \cos\Lambda \frac{\partial \Gamma}{\partial y'} \tag{63}$$

$$\frac{\partial \Gamma}{\partial x} = \frac{\partial \Gamma}{\partial x'}\frac{\partial x'}{\partial x} + \frac{\partial \Gamma}{\partial y'}\frac{\partial y'}{\partial x} = \cos\Lambda \frac{\partial \Gamma}{\partial x'} + \sin\Lambda \frac{\partial \Gamma}{\partial y'} \tag{64}$$

Substituting $\frac{\partial \Gamma}{\partial x'}$ from Eq. (64) into Eq. (63) results in

$$\frac{\partial \Gamma}{\partial y} = -\tan\Lambda \frac{\partial \Gamma}{\partial x} + \frac{1}{\cos\Lambda}\frac{\partial \Gamma}{\partial y'} \tag{65}$$

Since $\frac{\partial \Gamma}{\partial x} = -\gamma_y(x,y)$, $\frac{\partial \Gamma}{\partial y}$ or γ_x can be obtained through Eq. (65) if $\frac{\partial \Gamma}{\partial y'}$ can be computed. In the present method, $\frac{\partial \Gamma}{\partial y'}$ has been obtained by a trigonometric interpolation formula developed in Appendix D.

(b) Tip Suction

The tip suction can be predicted by using the trigonometric interpolation formula for $\frac{\partial \Gamma}{\partial y'}$ developed above. The tip suction per unit length of the tip chord is given by (Ref. 18)

$$s_t(x) = \pi \rho G^2(x) \tag{66}$$

where G(x) is the singularity parameter of $\Gamma(y)$ at the tip and is related to $\Gamma(y)$ by

$$G(x) = \sqrt{\frac{b}{2}} \lim_{y \to \frac{b}{2}} \sqrt{1 - \frac{y}{b/2}}\ \frac{1}{2}\frac{\partial \Gamma}{\partial y} \tag{67}$$

The detail of computing G(x) by using the trigonometric interpolation formula developed in Appendix D is formulated in Appendix E.

(c) β -derivatives

The distribution of lifting pressure coefficients can be written in terms of the wing upper surface perturbed velocity as (Ref. 19)

$$\Delta C_p = 4\frac{\partial \phi}{\partial x'} \tag{68}$$

where x' is measured along the freestream in sideslip (see Fig. 5). For small sideslip angle $\bar{\beta}$, Eq. (68) can be written as, by using Eqs. (62) with Λ replaced by $\bar{\beta}$,

$$\Delta C_p = 4\left(\frac{\partial\phi}{\partial x} - \bar{\beta}\frac{\partial\phi}{\partial y}\right) = 2\left(\gamma_y - \bar{\beta}\gamma_x\right) \tag{69}$$

The change in the lifting pressure in sideslip results from the wing-body interaction with or without dihedral (see the boundary conditions (26) and (29)) in sideslip and the term $-\bar{\beta}\gamma_x$ in Eq. (69), where γ_x is from the symmetrical loading. The second term can also be explained by Kutta-Joukowski theorem in that the sideslipping velocity will interact with the streamwise vortices (γ_x) to produce the positive lifting pressure on the right wing in positive lift. On the left wing, the lifting pressure is negative, thus creating a rolling moment. Hence, the rolling moment coefficient due to sideslip ("dihedral effect") can be calculated as

$$C_{l_\beta} = \frac{\partial C_l}{\partial \bar{\beta}} = -\frac{2}{S_w b}\int_{\text{right wing}}\left(\frac{\partial\gamma_y}{\partial\bar{\beta}} + \gamma_x\right)\cos\bar{\theta}\, y\, dS \tag{70}$$

where γ_x is regarded positive if as a vector it is printing downstream, $\partial\gamma_y/\partial\bar{\beta}$ is due to the wing-body interaction with or without dihedral and $\bar{\theta}$ the camber angle (including flaps) for proper force resolution.

To compute the wing contribution to C_{y_β} and C_{n_β}, the change in the wing edge forces with the sideslip must be found. For a wing with dihedral, or a wing-body combination with or without dihedral, an antisymmetrical pressure loading will be induced. This will change the wing edge forces. The sectional leading-edge thrust coefficient in combined symmetrical and antisymmetrical loadings can be written as

(Ref. 7):

$$\Delta C_x = -\frac{\pi}{2}\sqrt{1-M_\infty^2\cos^2\Lambda_\ell}\;\frac{(C_s+C_a)^2}{\cos\Lambda_\ell} \tag{71}$$

where C_s is the leading-edge singularity parameter in the symmetrical loading and the subscript "a" denotes the antisymmetrical case. It follows that

$$\Delta C_{x_\beta} = -\frac{\pi}{2}\sqrt{1-M_\infty^2\cos^2\Lambda_\ell}\;\frac{2C_s C_{a_\beta}}{\cos\Lambda_\ell} \tag{72}$$

where the subscript β denotes differentiation with respect to the sideslip angle. C_a can be computed in exactly the same way as in computing C_s. With $\Delta c_{x\beta}$ obtained, $\Delta C_{y\beta}$ is given by

$$\Delta C_{y_\beta} = \Delta C_{x_\beta}\tan\Lambda_\ell \tag{73}$$

The total contribtuion to $C_{y\beta}$ and $C_{n\beta}$ can be computed by integration . In addition, the incremental pressure loading due to sideslip will produce antisymmetrical change in the tip suction. According to Eq. (66), the tip suction can be written as

$$S_t = \pi\rho(G_s \pm G_a)^2$$

where the plus sign is for the right wing; the subscript s denotes the symmetrical loading and a for the antisymmetrical loading. It follows that

$$\frac{\partial S_t}{\partial\bar{\beta}} = 2\pi\rho G_s\left(\pm\frac{\partial G_a}{\partial\bar{\beta}}\right) \tag{74}$$

where $\frac{\partial G_a}{\partial\bar{\beta}}$ can be obtained in the same manner as G_s. Therefore, the wing side force due to sideslip will be contributed from the following sources:

(1) Contribution from the change in the leading-edge suction

$$\Delta C_{y_\beta} = \frac{2}{S_w}\int_{\text{right wing}} c(y)\,\Delta C_{y_\beta}\,dy \tag{75}$$

This is shown in Fig. 6(a)

(2) Contribution from the incremental pressure force

This is illustrated in Fig. 6(b), where it shows that with the lifting pressure acting normal to the planform, there will be a component of the pressure force contributing to the negative side force.

(3) Contribution from the induced drag (page 14-3, Ref. 20)

The induced drag is assumed to act in the direction of the freestream with sideslip. This is illustrated in Fig. 6(c). Hence, if C_{Di} is the induced drag due to the symmetrical loading, then

$$\Delta C_y = -C_{Di}\,\bar{\beta}$$

$$\Delta C_{y\beta} = -C_{Di} \qquad (76)$$

Of course, the viscous drag will also contribute to $C_{y\beta}$. But this is neglected here.

(4) Contribution from the Tip Suction

This is given by Eq. (74)

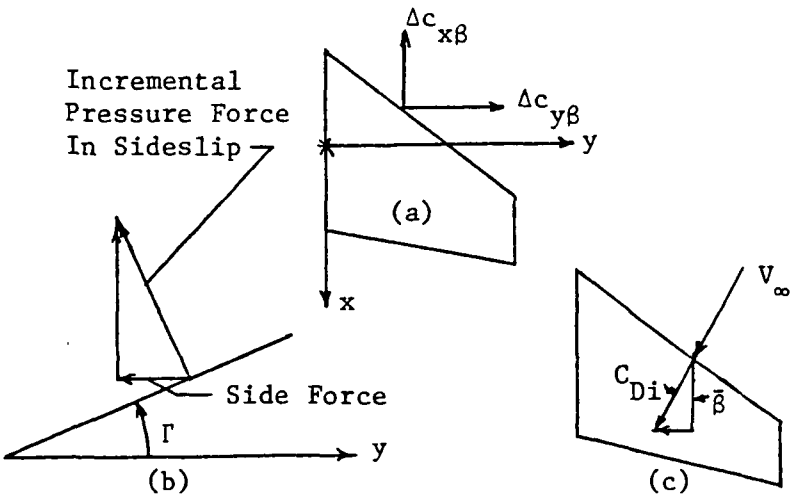

Figure 6 Wing Contribution to Side Force

Similarly, the wing contribution to the yawing moment due to sideslip results from the following sources:

(1) Contribution from the change in the leading-edge suction. This can be seen from Fig. 6(a). By taking moment of the forces $\Delta c_{x\beta}$ and $\Delta c_{y\beta}$ about the z-axis, $\Delta C_{n\beta}$ can be obtained.

(2) Contribution from the incremental pressure force

The incremental lifting pressure force, being assumed to act normal to the camber surface, will be resolved in a direction parallel to the chord plane. After multiplying by the moment arm y and integrating, the contribution to $C_{n\beta}$ can be obtained. In addition, the side force due to the dihedral shown in Fig. 6(b) will also contribute to $C_{n\beta}$.

(3) Contribution from the tip suction given by Eq. (74)

The fuselage contribution to the side force and yawing moment can be calculated in the same manner as in computing $C_{N(f)}$ and $C_{m(f)}$ due to fuselage. In the present case, the sectional side force coefficient is given by (see Fig. 4).

$$C_{y(f)} = -\frac{1}{r}\int_0^{2\pi} C_{p(f)}(r\,d\theta)\sin\theta \tag{77}$$

Therefore, $C_{y(f)}$ and $C_{n(f)}$ are computed as

$$C_{Y(f)} = \frac{1}{S_w}\int_{x_{fl}}^{x_p} r\,C_{y(f)}\,dx \tag{78}$$

$$C_{n(f)} = -\frac{1}{S_w b}\int_{x_{fl}}^{x_p} r\,C_{y(f)}\,x\,dx \tag{79}$$

Since the fuselage surface pressure $C_{p(f)}$ is computed at $\bar{\beta}$=5°, the results

of Eqs. (78) and (79) will be divided by $\bar{\beta}$ to obtain the fuselage contribution to $C_{y\beta}$ and $C_{n\beta}$.

(d) p-derivatives

The roll damping derivative $C_{\ell p}$ is computed by integrating the antisymmetrical pressure force induced by the roll rate multiplied by the spanwise moment arm, assuming that $pb/2V_\infty = 1$. The pressure force distribution is antisymmetrical, because with the positive roll rate, the right wing will see incremental upwash, while the left wing will be subject to incremental downwash. This can also be seen from the boundary condition Eq. (28), where y is positive for the right wing and negative for the left wing.

The side force and yawing moment due to roll rate, C_{yp} and C_{np}, respectively, are assumed to be due to the pressure distribution on the wing surface only. In other words, the fuselage contribution is ignored. Of course, the wing-body interaction has been included. The contribution to C_{yp} and C_{np} results from the following sources:

(1) Contribution from the change in the leading-edge suction

The incremental sectional leading-edge thrust coefficient is given by Eq. (72) with appropriate changes:

$$\Delta C_{xp} = -\frac{\pi}{2}\sqrt{1 - M_\infty^2 \cos^2\Lambda_\ell}\,\frac{2C_s C_{ap}}{\cos\Lambda_\ell} \tag{80}$$

where Δc_{xp} and C_{ap} are the derivatives with respect to $(pb/2V_\infty)$. Again, ΔC_{yp} is obtained from

$$\Delta C_{yp} = \Delta C_{xp} \tan\Lambda_\ell \tag{81}$$

With ΔC_{xp} and ΔC_{yp} known, their contribution to C_{yp} and C_{np} can be obtained by following the same procedure described previously for

$C_{y\beta}$ and $C_{n\beta}$.

(2) Contribution from the tip suction

The idea expressed in Eq. (74) is still applicable for this case.

(3) Contribution from the incremental pressure distribution

This contribution is non-zero if the dihedral angle is not zero (to both C_{yp} and C_{np}) and if the camber is present (to C_{np}). The concept described in relation to $C_{y\beta}$ and $C_{n\beta}$ is still applicable.

(e) r-derivatives

The incremental pressure distribution due to yaw rate consists of three components.

(1) Due to yawing, a backwash ry is produced (see Fig. 2). This will interact with the symmetrical γ_y to reduce the lifting pressure on the right wing:

$$\Delta C_{pr} = -\frac{ry}{V_\infty}\gamma_y\Big|_{rb/2V_\infty=1} = -\frac{2y}{b}\gamma_y \tag{82}$$

(2) The sidewash rx will interact with the symmetrical γ_x to produce the following ΔC_{pr}:

$$\Delta C_{pr} = -\frac{rx}{V_\infty}\gamma_x\Big|_{rb/2V_\infty=1} = -\frac{2x}{b}\gamma_x \tag{83}$$

(3) Wing-body interaction with or without dihedral. See the boundary conditions (27) and (30).

With the incremental antisymmetrical pressure distribution obtained, the wing rolling moment due to yawing can be computed immediately.

The calculation of C_{yr} and C_{nr} follows the same procedure of

computing $C_{y\beta}$ and $C_{n\beta}$ by recognizing the fact that a wing in yawing will produce the "variable sideslip" effect, because the sidewash varies on the wing and the fuselage.

4. Numerical Results and Discussions

4.1 Fuselage alone

In computing the fuselage surface pressure, Eq. (43) is used with the following modification. Since the theory is a linear one, near the nose the pressure would be unrealistic. This can be seen from the second term in Eq. (43), where $\frac{dR}{dx}$ could be infinitely large near the nose. Therefore, this term is modified to be

$$\cos\alpha \frac{dR}{dx} \quad \text{Replaced by} \quad (\cos\alpha + u) \frac{\frac{dR}{dx}}{\sqrt{1+\left(\frac{dR}{dx}\right)^2}} \tag{84}$$

This modification is similar to the Riegels factor used in the airfoil theory (Ref. 21). Figs 7-9 show the camparison of the pressure distribution. Except very near the nose, the present method appears to be reasonable in predicting the pressure distribution as compared with the experiment (Ref. 22). It should be noted that without the modification indicated in Eq. (84), the pressure within about 10% of the nose would be more negative than that presented in the figures.

4.2 Wing or Wing-body characteristics without jet interaction

It is well-known that the fuselage interaction will increase the loading on the wing. Fig. 10 shows the comparison of the predicted incremental loading with experimental results given in Reference 23. The present results were computed by including up to second-order Fourier modes in satisfying the fuselage boundary condition (i.e., n=2 in Eq. 6). The agreement is good except near the wing-body juncture.

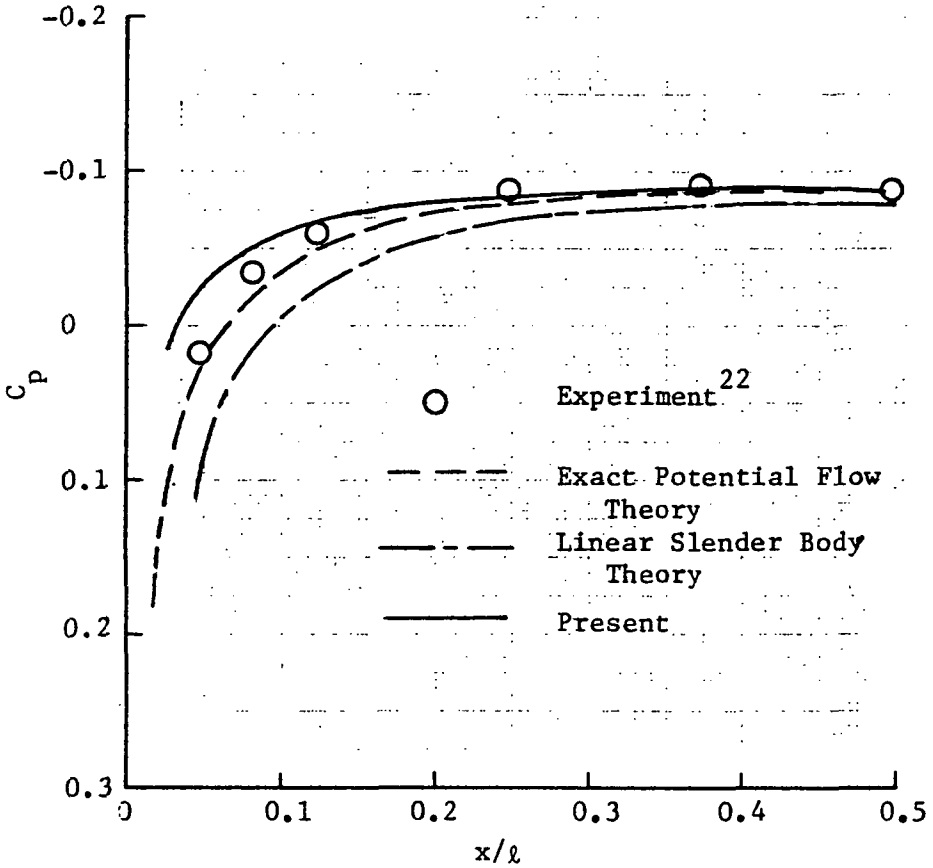

Figure 7. Comparison of Experimental and Theoretical Pressures on a Prolate Spheroid of Fineness Ratio 6 at $\alpha = 0$ and $M_\infty = 0$.

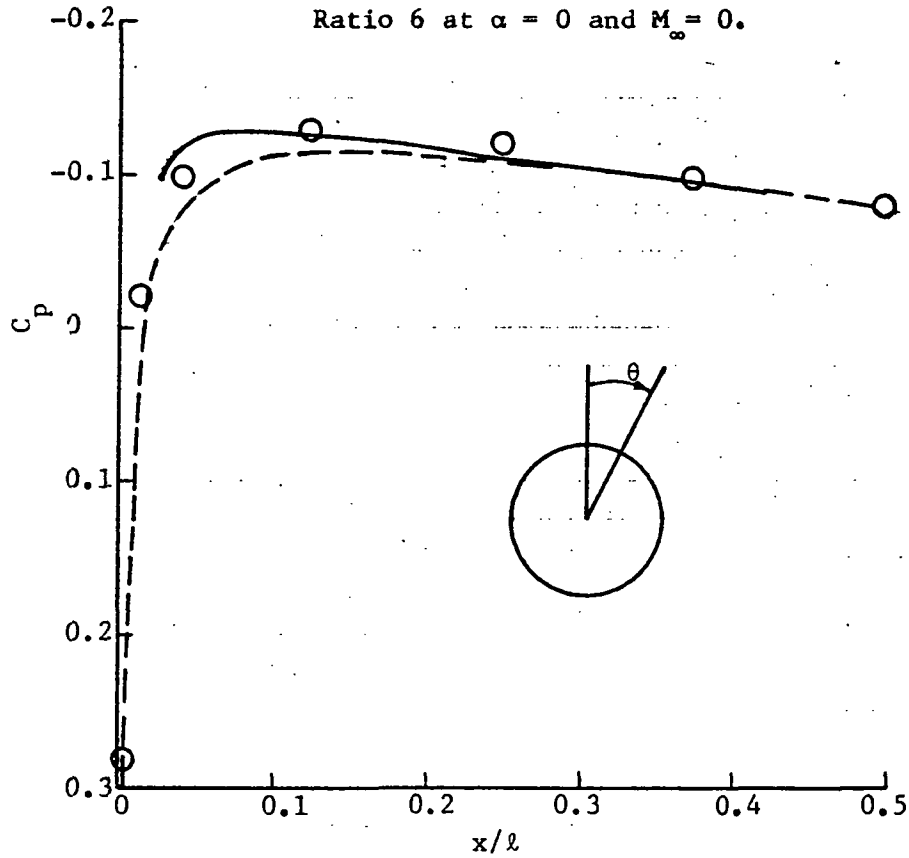

Figure 8. Comparison of Experimental and Theoretical Pressures on a Prolate Spheroid of Fineness Ratio of 6 at $\alpha = 5.6°$ and $M_\infty = 0$, $\theta = 0°$.

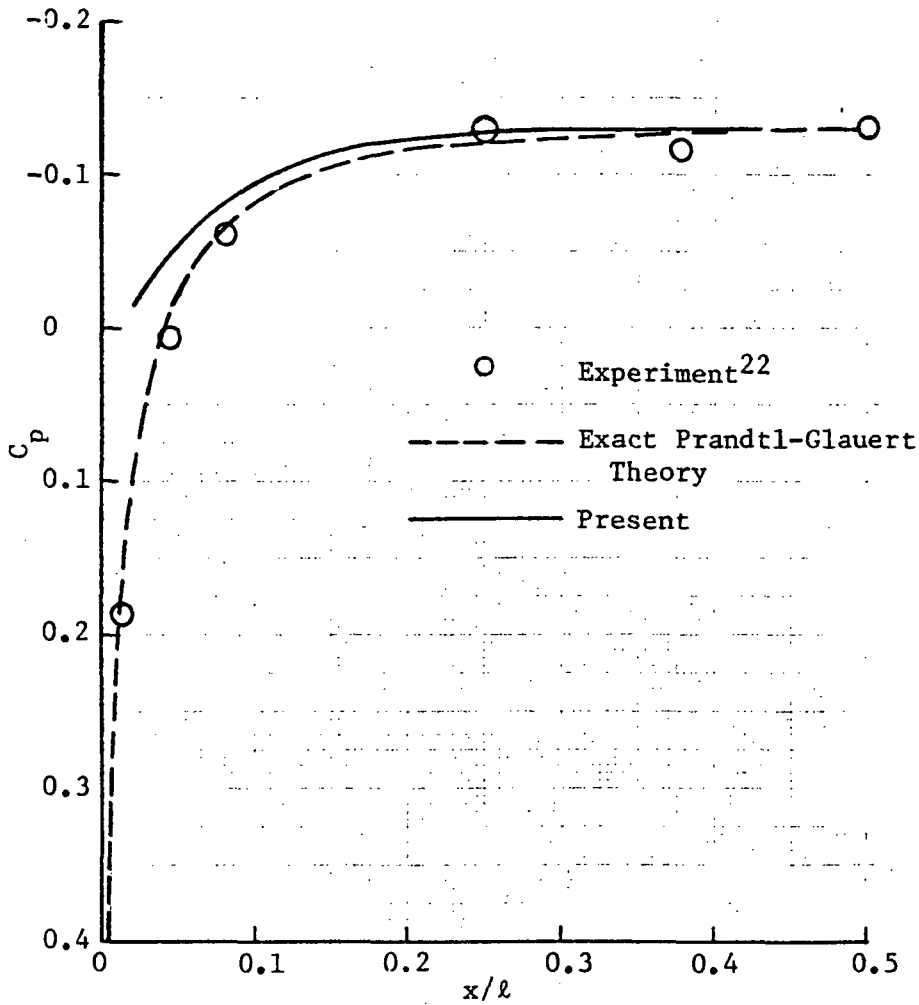

Figure 9. Comparison of Experimental and Theoretical Pressures on a Prolate Spheroid of Fineness Ratio 6 at $\alpha = 5.6°$, $M_\infty = 0.7$ and $\theta = 90°$.

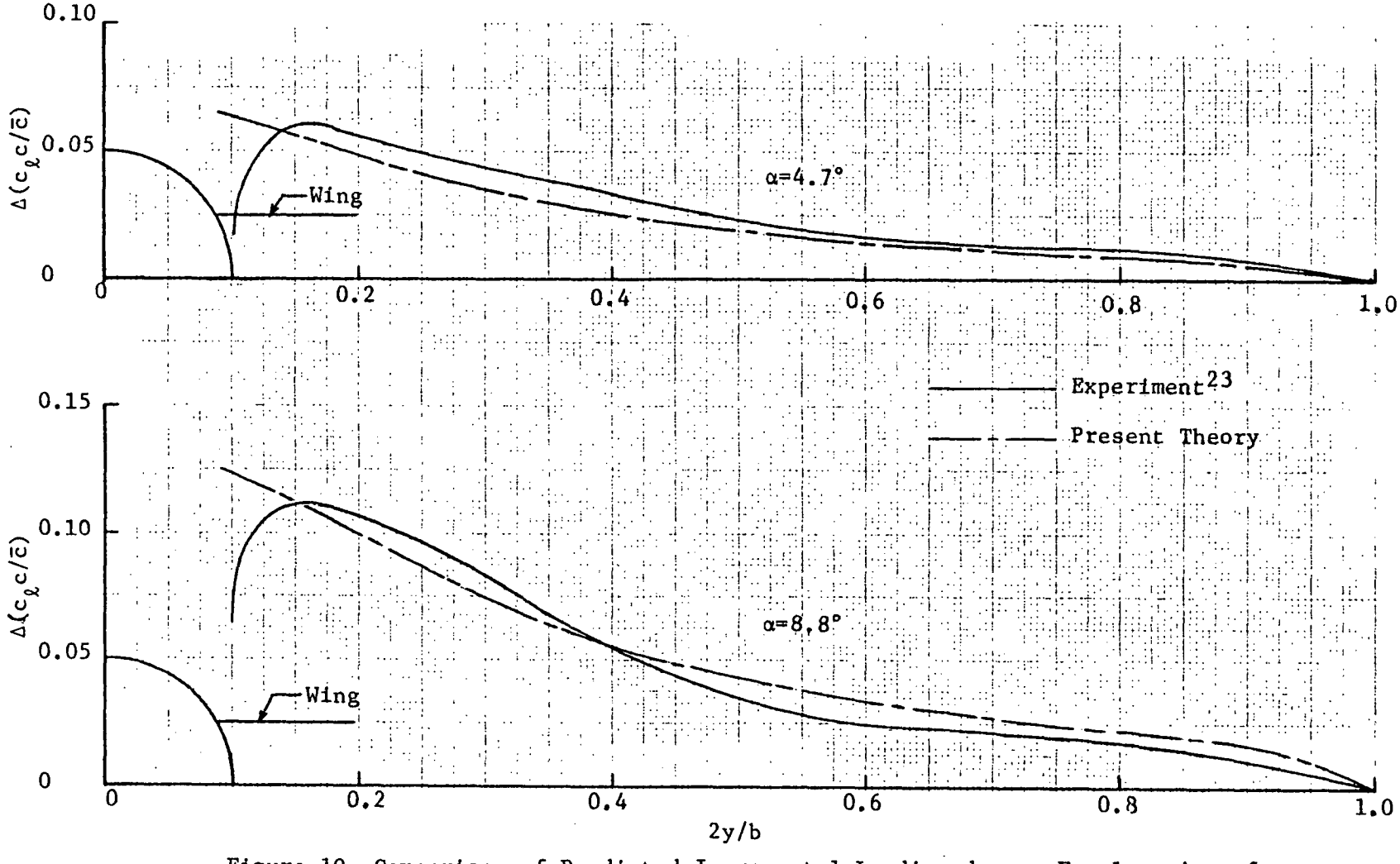

Figure 10. Comparison of Predicted Incremental Loading due to Fuselage interference with Experiment. High-wing Configuration with Fuselage Fineness Ratio of 10.

Before comparing the prediction of lateral-directional stability derivatives, it is necessary to make certain that the tip suction prediction is accurate, as the C_y - and C_n - derivatives depend on it. For this purpose, a cropped delta wing of aspect ratio 1.333 and taper ratio 0.5 is chosen. The present method is formulated in Appendix E. The present results are compared with Reference 18 in Table 1. It is seen that the agreement is good and the present method yields reasonably stable value with respect to the vortex arrangement.

With the accuracy of the tip suction prediction established, it is now possible to compare some of the predicted lateral-directional stability

Table 1. Comparison of Predicted Tip Suction Coefficient for a cropped Delta Wing of AR = 1.333 and λ =0.5.

α = 1 radian

N_C x N_S	Lamar 1.400	Present
5 x 20		1.361
7 x 20		1.377
9 x 20		1.387
5 x 12		1.364
7 x 12		1.384
9 x 12		1.395

derivatives. In Table 2, the p-derivatives for three wings are presented. The present results are seen to agree quite well with Garner's (Ref. 15). In Table 3, the predicted derivatives, $C_{\ell r}$ and $C_{\ell\beta}$, are compared with Queijo's method. Again, the agreement is reasonably good.

Finally, the results for a swept wing-body combination of Ref. 25 are presented in Fig. 11. $x'_{p/\ell}$, which is related to x_p in Eq. (46), is

taken to be 1. It is seen that $C_{\ell\beta}$ is well predicted, except at higher angles of attack. On the other hand, for $C_{n\beta}$, only the trend, not the absolute level, of the high-

Table 2. Comparison of Predicted p-Derivatives with Garner's Calculation (Ref. 15). Based on Body Axes.

Wing	Garner			Present		
	C_{y_p}/α	$C_{\ell p}$	C_{np}/C_L	C_{yp}/α	$C_{\ell p}$	C_{np}/C_L
Rectangular, AR=4, M_∞=0	1.374	-0.3360	-0.168	1.391	-0.3367	-0.171
Rectangular, AR=4, M_∞=0.866	1.945	-0.3794	-0.140	1.963	-0.3802	-0.145
Tapered-Swept, AR=2, Λ_ℓ=60° M_∞=0.7806	2.733	-0.1854	-0.365	2.6027	-0.1848	-0.336

Table 3. Comparison of Predicted Derivatives with Queijo's method. Based on Body Axes.

Derivatives	Queijo		Present
	Ref. 14	Ref. 24	
$C_{\ell r}/C_L$	0.4		0.384
$C_{\ell\beta}/C_L$		-0.47	-0.485

wing configuration is predicted. For the low-wing configuration, the predicted results at low angles of attack are more negative than the experimental values. The $C_{y\beta}$ derivative, not shown, follow the same trend of $C_{n\beta}$. In other words, for the high wing configuration, the trend of $C_{y\beta}$ is well predicted, but the predicted level is only about half of the experimental values. The discrepancy is most likely due to the effect of nonlinear lift and moment on the fuselage as discussed in Reference 13. The difference in $C_{y\beta}$ and $C_{n\beta}$ for high and low wing

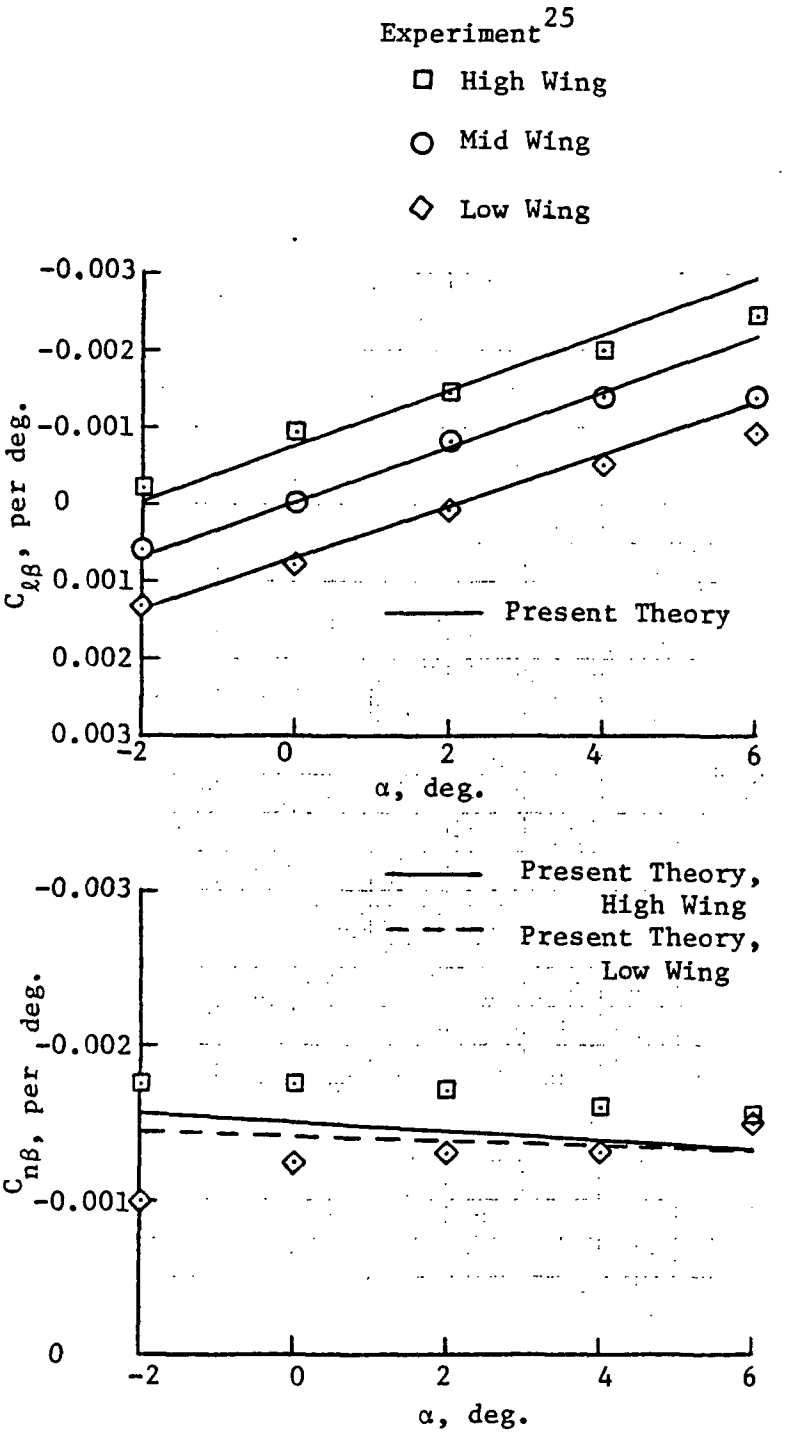

Figure 11. Effect of Wing Locations on the Sideslip Derivatives

configurations may have resulted from the wake displacement and deformation. However, this can not be proved in the present investigation.

4.3 Effect of Jet Interaction

The experimental results on the lateral-directional stability derivatives with jet effect are scarce. When available, they are mostly for the complete configuration (Refs. 26, 27). In Ref. 26, some results with T-tail off are presented. However, the fuselage has its after body upswept. To compare with this set of data, it is assumed in the present theory that the fuselage is a body of revolution, with elliptical forebody, cylindrical section within the wing root chord and parabolic after body. The maximum diameter is obtained by measurement of the graph, as the dimension of the fuselage is not given. From the model static test, the thrust efficiency can be determined to be 87%, and the jet deflection angle to be 44° at δ_f=60°. to predict C_L with the jet off as closely to the experimental values as possible at low angles of attack, the actual flap angle used in the program was assumed to be the same as the jet deflection angle, i.e., 44°. The predicted C_L is obtained by adding the computed incremental C_L due to jet effects to the experimental jet-off values. The results for the lift curves are shown in Fig. 12. It is seen that the lift is slightly overpredicted at C_T=3.6 and underpredicted at C_T=1.8 for the assumed configuration. The sideslip derivatives for the same configuration are presented in Fig. 13. The main difficulty in predicting $C_{y\beta}$ and $C_{n\beta}$ in the present case is that because of the upsweep of the fuselage after body, the flow separation would occur earlier than the case with a body of revolution. In the present computation, x'_p/ℓ is taken to be 0.8. The agreement is seen not as good as that shown on Fig. 11, in particular, for the dihedral

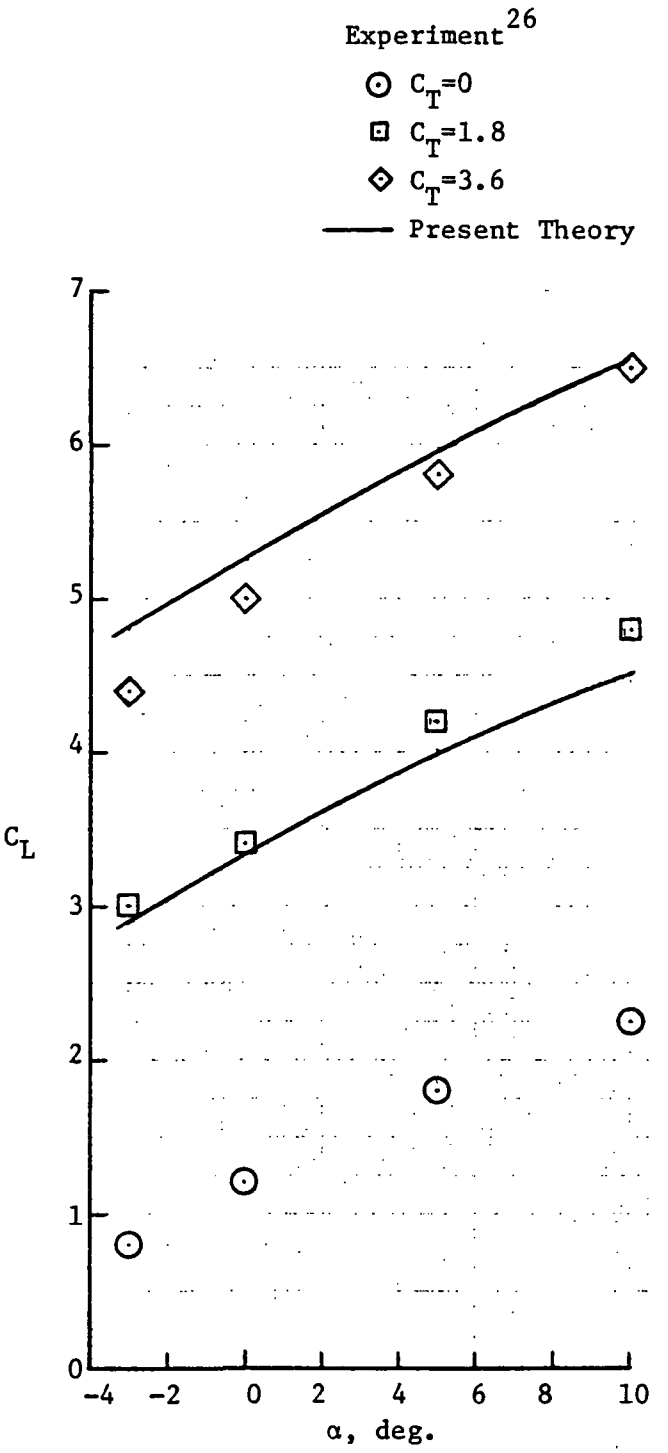

Figure 12. Comparison of Predicted Lift Curves with Experiment for an USB Configuration. δ_f=60°.

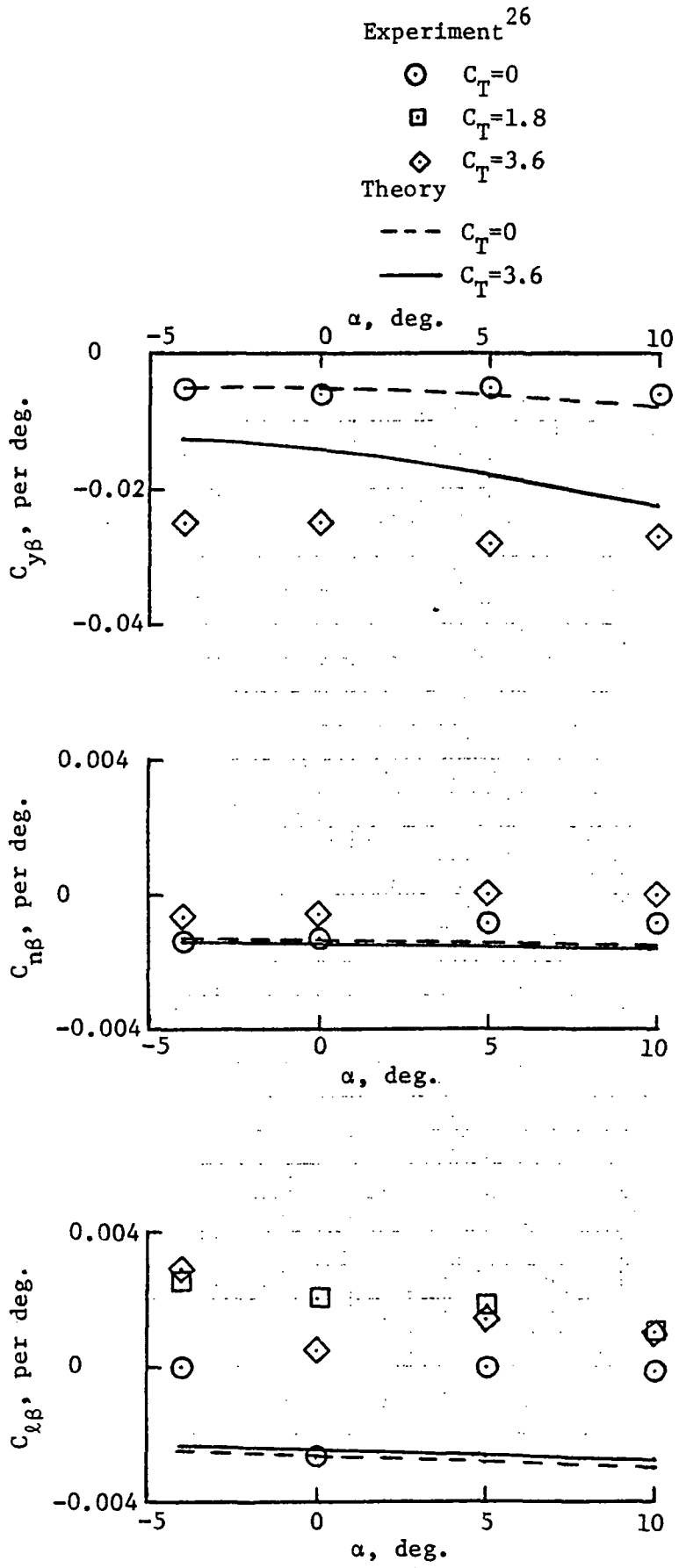

Figure 13. Comparison of Predicted Sideslip Derivatives with Experiment for an USB Configuration, δ_f=60°.

effect. The exact reason for the disagreement is not known. From the theoretical point of view, $C_{\ell\beta}$ for this high-wing configuration can be positive only if the symmetrical lift is negative. However, some experimental values are positive. In addition, the experimental results with the jet on are not consistent in that at $\alpha=0°$, with the power reduced, the value of $C_{\ell\beta}$ does not come closer to the jet-off values. It seems that some nonlinear viscous effect may have been present under the high lift conditions. The theory has a tendency to overpredict $C_{\ell\beta}$ at high lift, as can be seen from Fig. 11. It should be noted that the direct power effect due to the momentum transfer at the engine inlets on $C_{y\beta}$ and $C_{n\beta}$ is not included in the figure. When it is included, both $C_{y\beta}$ and $C_{n\beta}$ will be more negative. However, the uncertain contribution from the nacelles and fuselage will make this refinement unnecessary.

As indicated in Ref. 1, the swept wing configurations with the USB jet have unsatisfactory Dutch roll characteristics. Therefore, it is of interest to see how the leading-edge sweep will affect the lateral-directional stability derivatives. For this purpose, the unswept high-wing configuration of Ref. 26 is again used, with the leading-edge sweep angle increased to 30° without changing the aspect ratio. The results are plotted against the circulation lift coefficient in Figs. 14-16. Only those derivatives which show significant changes are presented. A general observation of the results is that although the circulation lift coefficient is greatly increased with the jet on, those lift-dependent derivatives are not proportionally changed for this configuration. It is seen that the swept wing configuration has better directional stability (more positive $C_{n\beta}$) with or without the jet on than the unswept one, and has large

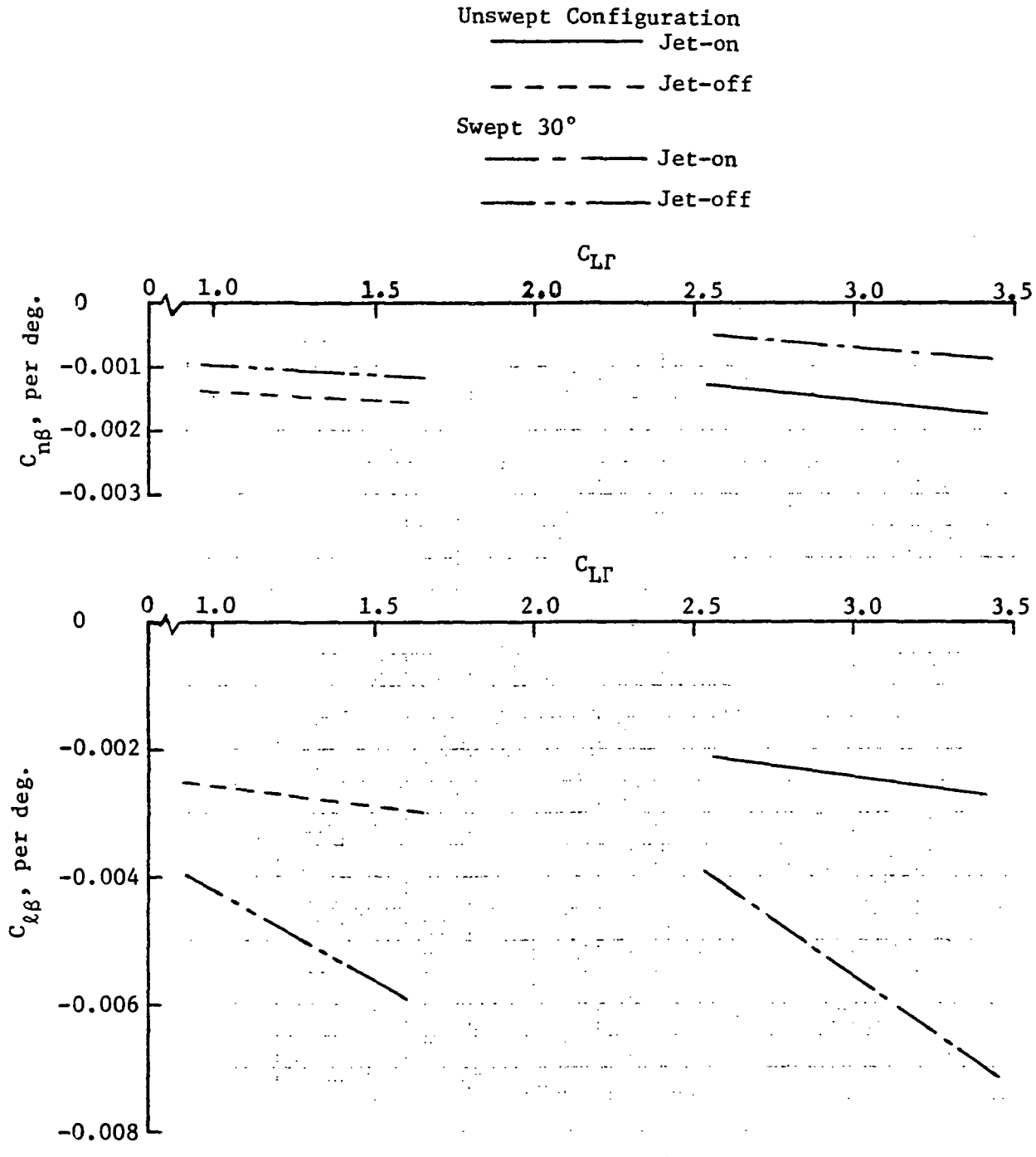

Figure 14. Theoretical Sideslip Derivatives for the Configuration of Ref. 26 with Different Leading-Edge Sweep Angles. C_T=3.6, δ_f=60° and Γ=5°.

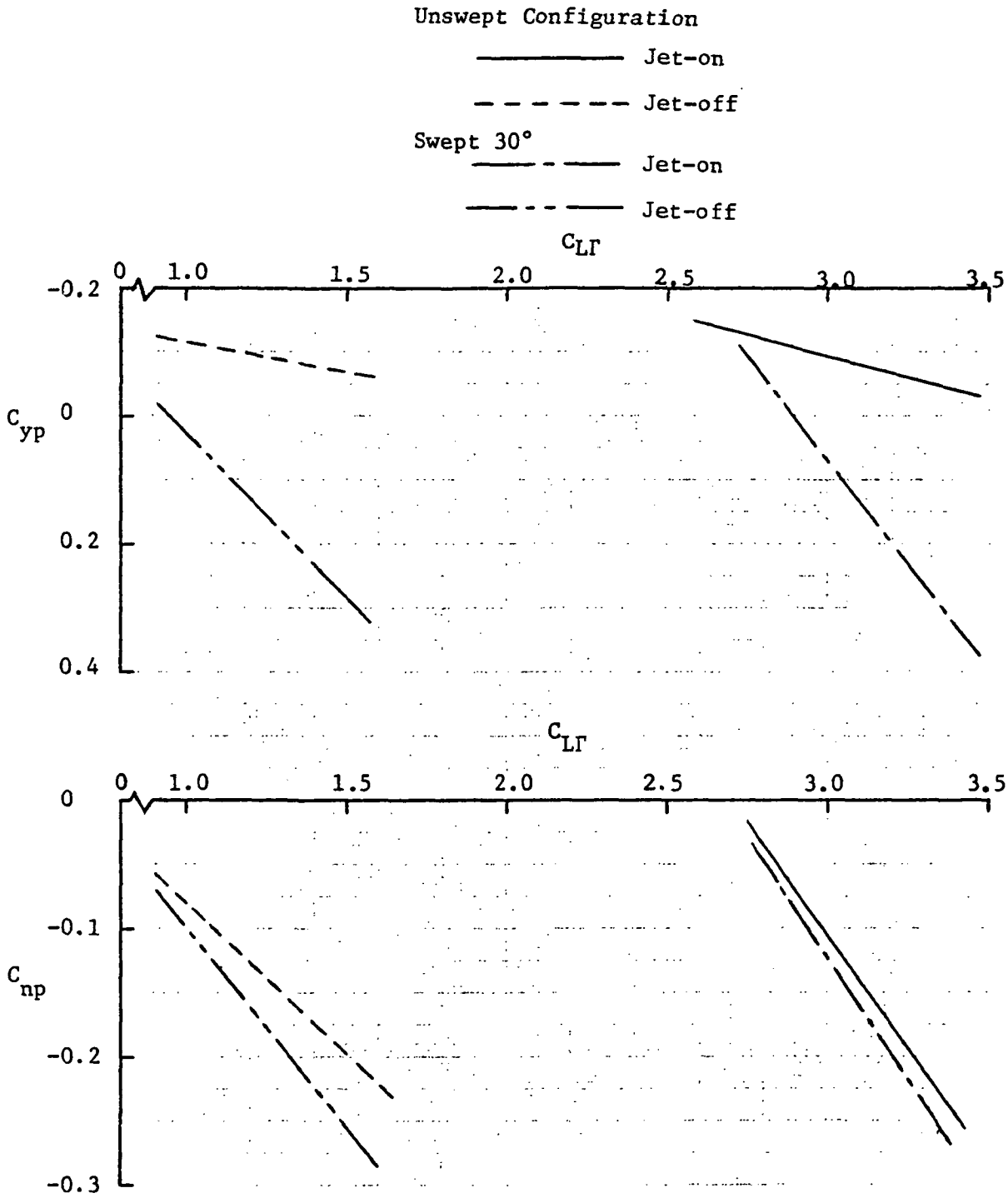

Figure 15. Theoretical Roll Derivatives for the Configuration of Ref. 26 with Different Leading-Edge Sweep Angles. C_T=3.6, δ_f=60° and Γ=5°.

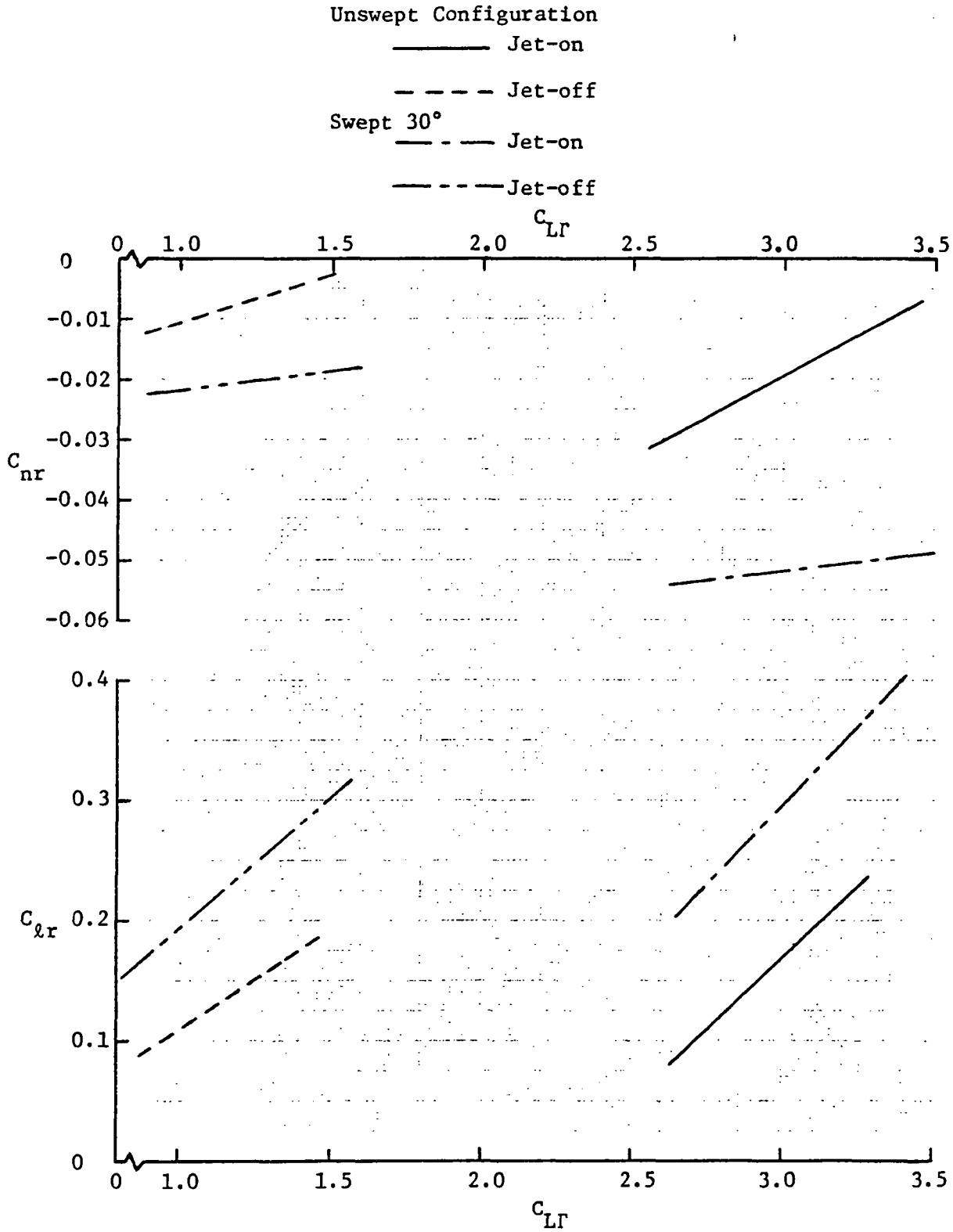

Figure 16. Theoretical Yaw Derivatives for the Configuration of Ref. 26 with Different Leading-Edge Sweep Angles. C_T=3.6, δ_f=60° and Γ=5°.

dihedral effect. The sweep largely increases C_{y_p}, mainly because of the contribution from the leading-edge suction. C_{n_p} is more negative at a given $C_{L\Gamma}$. From Fig. 16, it is seen that the leading-edge sweep provides better yaw damping (more negative C_{n_r}), and has large C_{ℓ_r}. Large positve C_{ℓ_r} is detrimental to the spiral mode, but more negative C_{n_r} is favorable. From the above results, it is seen that the unsatisfactory Dutch roll mode of the swept wing configuration is caused by the large dihedral effect without power. With the power on, the dihedral effect is further increased and makes the situation worse.

5. Concluding Remarks.

A jet interaction theory for calculating the lateral-directional stability derivatives for wing-body combinations has been developed. The fuselage effect is represented by the axial distribution of G.N. Ward's vortex multiplets. The predicted results show good agreement with experiment and other available theoretical methods for configurations without the jet effect. Because of lack of data for comparison, the accuracy of the theory with the blowing jet effect cannot be established. Further comparison with available data in the future would be needed if the refinement of the theory is to be made.

6. References

1. Campbell, J.P., "Overview of Powered-Lift Technology", in Powered-Lift Aerodynamics and Acoustics, NASA SP-406, 1976.

2. Roskam, J., "Flight Dynamics of Rigid and Elastic Airplanes", Part One, published by Roskam Aviation and Engineering Corporation, 519 Boulder, Lawrence, Kansas.

3. Lan, C.E.; Fillman, G.L. and Fox, C.H. Jr., "Computer Program for Calculating Aerodynamic Characteristics of Upper-Surface-Blowing and Over-Wing-Blowing Configurations", NASA TM X-73987, Feb. 1977.

4. Ashley, H. and Rodden, W.P., "Wing-Body Aerodynamic Interaction", Annual Review of Fluid Mechanics, Vol.4, 1972.

5. Tulinius, J.R., "Theoretical Prediction of Thick Wing and Pylon-Fuselage-Fanpod-Nacelle Aerodynamic Characteristics at Subcritical Speeds", NASA CR-137578, July, 1974.

6. Dusto, A. R., et al. "A Method for Predicting the Stability Characteristics of Control Configured Vehicles", Vol. I, AFFDL-TR-74-91, Nov. 1974.

7. Lan, C.E., "A Quasi-Vortex-Lattice Method in Thin Wing Theory", J. Aircraft, Vol. 11, No. 9, Sept. 1974, pp. 518-527.

8. Lan, C.E., and Campbell, J.F., "A Wing-Jet Interaction Theory for USB Configurations", Journal of Aircraft, Vol. 13, No. 9, Sept. 1976, pp. 718-726.

9. Lan, C.E., "Theoretical Aerodynamics of Over-Wing-Blowing-Configurations", Journal of Aircraft, Vol. 14, No. 6, June 1977, pp. 517-518.

10. Ward, G. N., "Linearized Theory of Steady High-Speed Flow", Chapter 9, Cambridge University Press, 1955.

11. Liepmann, H. W. and Roshko, A., "Elements of Gasdynamics", Chapter 9, Wiley, 1963.

12. Lan, C. E. and Campbell, J. F., "Theoretical Aerodynamics of Upper-Surface-Blowing Jet-Wing Interaction", NASA TN D-7936, Nov. 1975.

13. Hopkins, E. J., "A Semiempirical Method for Calculating the Pitching Moment of Bodies of Revolution at Low Mach Numbers", NACA RMA51C14, 1951.

14. Queijo, M. J., "Theory for Computing Span Loads and Stability Derivatives due to Sideslip, Yawing, and Rolling for Wings in Subsonic Compressible Flow", NASA TN D-4929, Dec. 1968.

15. "On the Application of Subsonic Linearized Wing Theory to Second-Order Forces and Moments", ARC R&M No. 3758, 1975. Part I General Principles and Mathematical Models, by G. J. Hancock. Part II Edge Forces and Roll-Rate Derivatives, by H. C. Garner.

16. Kálmán, T. P., Giesing, J. P. and Rodden, W. P., "Spanwise Distribution of Induced Drag in Subsonic Flow by the Vortex Lattice Method", Journal of Aircraft, Vol. 7, No.6, Nov.-Dec. 1970, pp. 574-576.

17. Hua, H. M., "A Finite-Element Method for Calculating Aerodynamic Coefficients of a Subsonic Airplane", Journal of Aircraft, Vol. 10, No. 7, July 1973, pp. 422-426.

18. Lamar, J. E., "Extension of Leading-Edge-Suction Analogy to Wings with Separated Flow Around the Side Edges at Subsonic Speeds", NASA TR R-428, Oct. 1974.

19. Margolis, K., Sherman, W. L. and Hannah, M. E., "Theroetical Calculation of the Pressure Distribution, Span Loading, and Rolling Moment due to Sideslip at Supersonic Speeds for Thin Sweptback Tapered Wings with Supersonic Trailing Edges and Wing Tips Parallel to the Axis of Wing Symmetry", NACA TN 2898, Feb. 1953.

20. Hoerner, S. F. and Borst, H. V., "Fluid-Dynamic Lift", by Hoerner Fluid Dynamics, P.O. Box 342, Brick Town, N. J. 08723, 1975.

21. Weber, J., "The Calculation of the Pressure Distribution Over the Surface of Two-Dimensional and Swept Wings with Symmetrical Aerofoil Sections", ARC R & M 2918, July 1953.

22. Matthews, C. W., "A Comparison of the Experimental Subsonic Pressure Distributions about Several Bodies of Revolution with Pressure Distributions Computed by means of the Linearized Theory", NACA Report 1155, 1953.

23. Martina, A. P., "The Interference Effects of a Body on the Spanwise Load Distributions of Two 45° Sweptback Wings of Aspect Ratio 8.02 from Low-Speed Tests", NACA TN 3730, August 1956.

24. Queijo, M.J., "Theoretical Span Load Distributions and Rolling Moments for Sideslipping Wings of Arbitrary Plan Form in Incompressible Flow", NACA Report 1269, 1956.

25. Goodman, A., "Effects of Wing Position and Horizontal-Tail Position on the Static Stability Characteristics of Models with Unswept and 45° Sweptback Surfaces with Some Reference to Mutual Interference", NACA TN 2504, Oct. 1951.

26. Phelps, A. E. III, "Wind-Tunnel Investigation of a Twin-Engine Straight-Wing Upper-Surface Blown Jet-Flap Configuration", NASA TN D-7778, 1975.

27. Parlett, L. P., "Free-Flight Wind-Tunnel Investigation of a Four-Engine Sweptwing Upper-Surface Blown Transport Configuration", NASA TM X-71932, 1974.

Appendix A

Influence Coefficient Matrices for Wing-Body-Jet Interaction

(1.) Effect of Fuselage on Wing

Consider a wing position on the fuselage as shown in Fig. A.1. At any point on the wing, the upwash induced by the fuselage can be shown to be

$$w = v_r \cos\theta - v_\theta \sin\theta \tag{A.1}$$

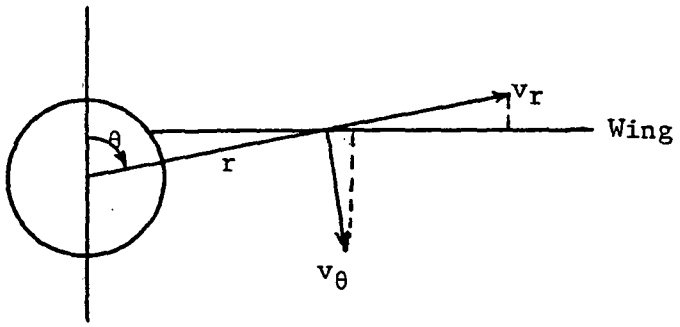

Figure A.1 Induced Velocity on Wing due to Fuselage

Using the formulation with G.N. Ward's vortex multiplets, v_r is given by Eq. (14)

$$v_r = \frac{\partial \phi_f}{\partial r} = -\frac{1}{4\pi} \sum_n \begin{Bmatrix} \cos n\theta \\ \sin n\theta \end{Bmatrix} \left\{ \left[\frac{\partial F_n}{\partial r}(x, r, x_{ft}) - \frac{\partial F_n}{\partial r}(x, r, x_{fl}) \right] f_n(x_{fl}) + \frac{l}{2} \frac{\pi}{N_F} \sum_k f'_{nk} \sin\theta_{lk} \left[\frac{\partial F_n}{\partial r}(x, r, x_{ft}) - \frac{\partial F_n}{\partial r}(x, r, \xi_k) \right] \right\} \tag{A.2}$$

where $l = x_{ft} - x_{fl}$, and $\cos n\theta$ is to be used for symmetrical cases and $\sin n\theta$ for antisymmetrical cases. To find v_θ, Eq.(2) is differentiated with respect to θ:

$$v_\theta = \frac{1}{r} \frac{\partial \phi_f}{\partial \theta} = -\frac{1}{4\pi} \frac{1}{r} \sum_n \begin{Bmatrix} -n\sin n\theta \\ n\cos n\theta \end{Bmatrix} \left\{ \left[F_n(x, r, x_{ft}) - F_n(x, r, x_{fl}) \right] f_n(x_{fl}) + \frac{l}{2} \frac{\pi}{N_F} \sum_k f'_{nk} \sin\theta_{lk} \left[F_n(x, r, x_{ft}) - F_n(x, r, \xi_k) \right] \right\} \tag{A.3}$$

In the above equations, F_n and $\frac{\partial F_n}{\partial r}$ are defined as follows:

$$F_n(x,r,\xi)=-\frac{1}{n}\frac{\left[x-\xi+\sqrt{(x-\xi)^2+\beta^2r^2}\,\right]^n}{r^n}\quad,\ n\neq 0 \tag{A.4}$$

$$\frac{\partial F_n}{\partial r}(x,r,\xi)=\frac{x-\xi}{r}\frac{\left[x-\xi+\sqrt{(x-\xi)^2+\beta^2r^2}\,\right]^n}{r^n\sqrt{(x-\xi)^2+\beta^2r^2}}\quad,\ n\geq 0 \tag{A.5}$$

Substituting Eqs. (A.2) and (A.3) into Eq. (A.1), the upwash expression due to each Fourier component can be obtained. For example, in the case of symmetrical loading, the upwash due to Fourier component n is

$$w^{(n)}=-\frac{\cos\theta}{4\pi}\begin{Bmatrix}\cos n\theta\\ \sin n\theta\end{Bmatrix}\left\{\left[\frac{\partial F_n}{\partial r}(x_{ft})-\frac{\partial F_n}{\partial r}(x_{f\ell})\right]f_n(x_{f\ell})+\frac{\ell}{2}\frac{\pi}{N_F}\sum_k{}'f'_{nk}\sin\theta_{lk}\cdot\right.$$
$$\left.\cdot\left[\frac{\partial F_n}{\partial r}(x_{ft})-\frac{\partial F_n}{\partial r}(\xi_k)\right]\right\}+\frac{\sin\theta}{4\pi}\frac{1}{r}\begin{Bmatrix}-n\sin n\theta\\ n\cos n\theta\end{Bmatrix}\left\{\left[F_n(x_{ft})-F_n(x_{f\ell})\right]f_n(x_{f\ell})\right.$$
$$\left.+\frac{\ell}{2}\frac{\pi}{N_F}\sum_k{}'f'_{nk}\sin\theta_{lk}\left[F_n(x_{ft})-F_n(\xi_k)\right]\right\} \tag{A.6}$$

where it is understood that $\frac{\partial F_n}{\partial r}(x_{ft})=\frac{\partial F_n}{\partial r}(x,r,x_{ft})$, etc.

The influence coefficient matrix $[N_{wf}^{(n)}]$ is then defined as

$$[N_{wf}^{(n)}]_{ik}=-\frac{\cos\theta_i}{4\pi}\begin{Bmatrix}\cos n\theta_i\\ \sin n\theta_i\end{Bmatrix}\frac{\ell}{2}\frac{\pi}{N_F}\sin\theta_{lk}\left[\frac{\partial F_n}{\partial r}(x_{ft})-\frac{\partial F_n}{\partial r}(\xi_k)\right]$$
$$+\frac{\sin\theta_i}{4\pi r_i}\begin{Bmatrix}-n\sin n\theta_i\\ n\cos n\theta_i\end{Bmatrix}\frac{\ell}{2}\frac{\pi}{N_F}\sin\theta_{lk}\left[F_n(x_{ft})-F_n(\xi_k)\right] \tag{A.7}$$

The term H_1 appearing in Eq. (24) is given by the remaining terms in Eq. (A.6) with $n=1$:

$$H_1 = -\frac{\cos\theta_i}{4\pi}\begin{Bmatrix}\cos n\theta_i \\ \sin n\theta_i\end{Bmatrix}\left[\frac{\partial F_1}{\partial r}(x_{f_t}) - \frac{\partial F_1}{\partial r}(x_{f_\ell})\right] f_1(x_{f_\ell}) +$$

$$+ \frac{\sin\theta_i}{4\pi r_i}\begin{Bmatrix}-n\sin n\theta_i \\ n\cos n\theta_i\end{Bmatrix}\left[F_1(x_{f_t}) - F_1(x_{f_\ell})\right] f_1(x_{f_\ell}) \qquad \text{(A.8)}$$

(2.) Effect of Fuselage on Jet

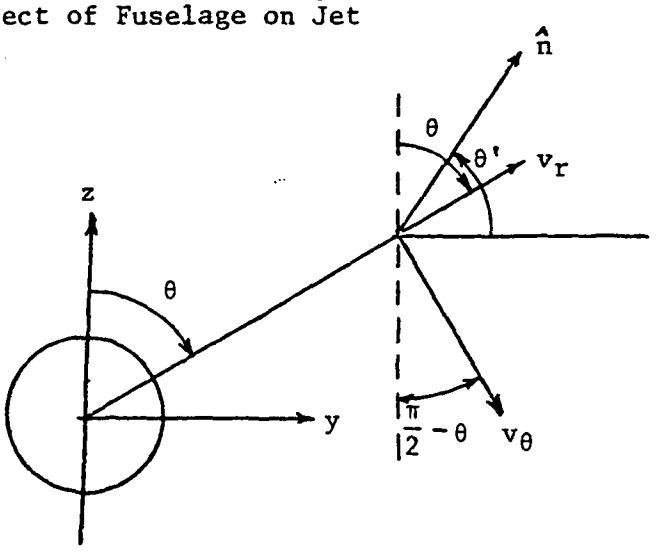

Figure A.2 Induced Velocity on Jet due to Fuselage

Referring to Fig. A.2 where $\hat{n}$ is the unit outward normal vector to the jet surface, it can be seen that

$$\hat{n} = \hat{j}\cos\theta' + \hat{k}\sin\theta' \qquad \text{(A.9)}$$

The velocity vector induced by the presence of the fuselage can be expressed in terms of v_r and v_θ as

$$\vec{v} = \hat{j}\left(v_r\sin\theta + v_\theta\cos\theta\right) + \hat{k}\left(v_r\cos\theta - v_\theta\sin\theta\right) \qquad \text{(A.10)}$$

It follows that the normal velocity component induced on the jet is given by

$$v_n = \vec{v}\cdot\hat{n} = (v_r \sin\theta + v_\theta \cos\theta)\cos\theta' + (v_r \cos\theta - v_\theta \sin\theta)\sin\theta' \quad \text{(A.11)}$$

With Eqs. (A.2) and (A.3) substituted into Eq. (A.11), the influence coefficient matrix $[N_{Jf}^{(n)}]$ can be obtained:

$$\begin{aligned}
[N_{Jf}^{(n)}]_{ik} = \Big\{ & -\frac{\sin\theta_i}{4\pi}\begin{pmatrix}\cos n\theta_i \\ \sin n\theta_i\end{pmatrix}\frac{l}{2}\frac{\pi}{N_F}\sin\theta_{ik}\left[\frac{\partial F_n}{\partial r}(x_{fk}) - \frac{\partial F_n}{\partial r}(\xi_k)\right] \\
& - \frac{\cos\theta_i}{4\pi r_i}\begin{pmatrix}-n\sin n\theta_i \\ n\cos n\theta_i\end{pmatrix}\frac{l}{2}\frac{\pi}{N_F}\sin\theta_{ik}\left[F_n(x_{fk}) - F_n(\xi_k)\right]\Big\}\cos\theta_i' \\
+ \Big\{ & -\frac{\cos\theta_i}{4\pi}\begin{pmatrix}\cos n\theta_i \\ \sin n\theta_i\end{pmatrix}\frac{l}{2}\frac{\pi}{N_F}\sin\theta_{ik}\left[\frac{\partial F_n}{\partial r}(x_{fk}) - \frac{\partial F_n}{\partial r}(\xi_k)\right] \\
& + \frac{\sin\theta_i}{4\pi r_i}\begin{pmatrix}-n\sin n\theta_i \\ n\cos n\theta_i\end{pmatrix}\frac{l}{2}\frac{\pi}{N_F}\sin\theta_{ik}\left[F_n(x_{fk}) - F_n(\xi_k)\right]\Big\}\sin\theta_i'
\end{aligned} \quad \text{(A.12)}$$

The term P_i in Eq. (34) is given by

$$\begin{aligned}
P_i = \Big\{ & -\frac{\sin\theta_i}{4\pi}\begin{pmatrix}\cos n\theta_i \\ \sin n\theta_i\end{pmatrix}\left[\frac{\partial F_i}{\partial r}(x_{fk}) - \frac{\partial F_i}{\partial r}(x_{fl})\right] f_i(x_{fl}) \\
& - \frac{\cos\theta_i}{4\pi r_i}\begin{pmatrix}-n\sin n\theta_i \\ n\cos n\theta_i\end{pmatrix}\left[F_i(x_{fk}) - F_i(x_{fl})\right] f_i(x_{fl})\Big\}\cos\theta_i' \\
+ \Big\{ & -\frac{\cos\theta_i}{4\pi}\begin{pmatrix}\cos n\theta_i \\ \sin n\theta_i\end{pmatrix}\left[\frac{\partial F_i}{\partial r}(x_{fk}) - \frac{\partial F_i}{\partial r}(x_{fl})\right] f_i(x_{fl}) \\
& + \frac{\sin\theta_i}{4\pi r_i}\begin{pmatrix}-n\sin n\theta_i \\ n\cos n\theta_i\end{pmatrix}\left[F_i(x_{fk}) - F_i(x_{fl})\right] f_i(x_{fl})\Big\}\sin\theta_i'
\end{aligned} \quad \text{(A.13)}$$

To find the u-influence coefficient matrix $[S_{Jf}^{(n)}]$, Eq. (2) is differentiated with x to give

$$\begin{aligned}
\frac{\partial \phi_f^{(n)}}{\partial x} = -\frac{1}{4\pi}\begin{pmatrix}\cos n\theta \\ \sin n\theta\end{pmatrix}\Big\{ & \left[\frac{\partial F_n}{\partial x}(x_{fk}) - \frac{\partial F_n}{\partial x}(x_{fl})\right] f_n(x_{fl}) + \\
& \frac{l}{2}\frac{\pi}{N_F}\sum_k f_{nk}'\sin\theta_{ik}\left[\frac{\partial F_n}{\partial x}(x_{fk}) - \frac{\partial F_n}{\partial x}(\xi_k)\right]\Big\}
\end{aligned} \quad \text{(A.14)}$$

where

$$\frac{\partial F_n}{\partial x}(x,r,\xi) = -\frac{1}{r^n}\frac{\left[x-\xi+\sqrt{(x-\xi)^2+\beta^2 r^2}\,\right]^n}{\sqrt{(x-\xi)^2+\beta^2 r^2}}\,,\quad n\geq 0 \tag{A.15}$$

$$\frac{\partial F_n}{\partial x}(x_{fi}) = \frac{\partial F_n}{\partial x}(x,r,x_{fi}) \tag{A.16}$$

It follows that the influence coefficient matrix $[S_{Jf}^{(n)}]$ is given by

$$[S_{Jf}^{(n)}]_{ik} = -\frac{1}{4\pi}\begin{pmatrix}\cos n\theta_i\\ \sin n\theta_i\end{pmatrix}\frac{\ell}{2}\frac{\pi}{N_f}\sin\theta_{ik}\left[\frac{\partial F_n}{\partial x}(x_{fi})-\frac{\partial F_n}{\partial x}(\xi_k)\right] \tag{A.17}$$

and D_1 in Eq. (33) is

$$D_1 = -\frac{1}{4\pi}\begin{pmatrix}\cos\theta_i\\ \sin\theta_i\end{pmatrix}\left[\frac{\partial F_1}{\partial x}(x_{fi})-\frac{\partial F_1}{\partial x}(x_{fl})\right]f_1(x_{fl}) \tag{A.18}$$

(2.) Effect of Wing-Jet on Fuselage

The general expression for the induced velocity at any point due to the wing-jet vortices has been given before (Ref. 8). Consider a unit horseshoe vortex "k" on the wing or the jet surface. At a fixed number of points to be specified on the fuselage circumference, both the upwash w and the sidewash v will be computed. The normal velocity at a given point at station i will be given by (see Fig. A.3)

$$v_n = w\cos\theta + v\sin\theta \tag{A.19}$$

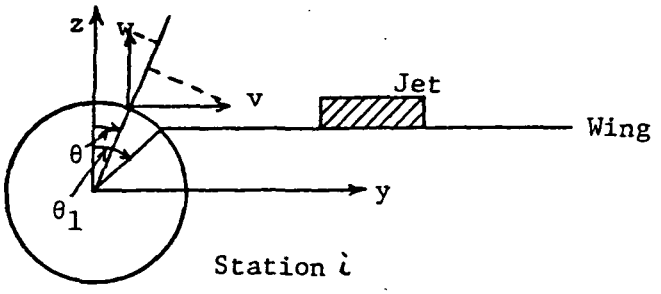

Figure A.3 Induced Velocity on Fuselage due to Wing-Jet Vortices

Let V_n be developed in a cosine or sine Fourier series without the zero order term, depending on whether it is a symmetrical or anti-symmetrical case:

$$V_n = \sum_{n=1} a_n \begin{cases} \cos n\theta \\ \sin n\theta \end{cases} \tag{A.20}$$

Then, the Fourier coefficients will be given by

$$a_n = \frac{2}{\pi} \int_0^{\pi} V_n \begin{Bmatrix} \cos n\theta \\ \sin n\theta \end{Bmatrix} d\theta \tag{A.21}$$

To illustrate the numerical integration, consider the integral

$$a_n = \frac{2}{\pi} \int_0^{\pi} V_n \cos n\theta \, d\theta$$

The interval $(0, \pi)$ will be divided into two parts: $(0, \theta_1)$ and (θ_1, π) (see Fig. A.3). Hence,

$$a_n = \frac{2}{\pi} \left\{ \int_0^{\theta_1} V_n \cos n\theta \, d\theta + \int_{\theta_1}^{\pi} V_n \cos n\theta \, d\theta \right\}$$

$$\cong \frac{2}{\pi} \left\{ \frac{\theta_1}{N_1} \sum_{\ell} V_{n\ell} \cos n\theta_\ell + \frac{\pi - \theta_1}{N_2} \sum_{j} V_{nj} \cos n\theta_j \right\} \tag{A.22}$$

where the integrals have been reduced to finite sums through the midpoint trapezoidal rule and

$$\theta_\ell = \frac{2\ell - 1}{2N_{f1}} \theta_1 \qquad , \ell = 1, \cdots, N_{f1} \tag{A.23}$$

$$\theta_j = \theta_1 + \frac{(2j-1)(\pi - \theta_1)}{2N_{f2}} \, , j = 1, \cdots, N_{f2} \tag{A.24}$$

The angular positions indicated by θ_ℓ and θ_j are the locations at which the induced velocities are to be computed. With a_n obtained, the influence coefficient matrices $[N_{fJ}^{(n)}]$ and $[N_{fW}^{(n)}]$ are then given by

$$[N_{fJ}^{(n)}]_{ik} \quad \text{or} \quad [N_{fW}^{(n)}]_{ik} = a_n \tag{A.25}$$

(3.) Effect on Fuselage due to Fuselage

The influence coefficient matrix $[N_{ff}^{(n)}]$ can be obtained from Eq. (A.2) as follows:

$$[N_{ff}^{(n)}]_{ik} = -\frac{1}{4\pi}\frac{\ell}{2}\frac{\pi}{N_F}\sin\theta_{ik}\left[\frac{\partial F_n}{\partial r}(x_i, R_i, x_{fk}) - \frac{\partial F_n}{\partial r}(x_i, R_i, \xi_k)\right] \tag{A.26}$$

where $R_i = R(x_i)$, the fuselage radius at x_i.

Appendix B

Derivation of $f_n(x_{fl})$ in the Formulation for the Fuselage Effect

(1.) The Expression for $f_0(x_{fl})$.

The zero-order Fourier component of the boundary condition Eq. (5) can be written as

$$\frac{\partial \phi_f}{\partial r} = \cos\alpha \frac{dR}{dx} \tag{B.1}$$

From Eq. (6), it is obtained that

$$-\frac{1}{4\pi}\left\{ f_0(x_{ft}) r \frac{\partial F_0}{\partial r}(x_{ft}) - f_0(x_{fl}) r \frac{\partial F_0}{\partial r}(x_{fl}) - \int_{x_{fl}}^{x_{ft}} r \frac{\partial F_0}{\partial r}(x, r, \xi) f_0'(\xi) d\xi \right\}_{r=R(x)}$$

$$= \cos\alpha \, R \frac{dR}{dx} \tag{B.2}$$

where the equation has been multiplied through with $r=R(x)$. Now, Eq. (B.2) will be evaluated at $x = x_{fl}$. According to Eq. (6) for the expression $\frac{\partial F_0}{\partial r}$, the following limiting values can be derived, assuming $R(x_{fl})=0$,

$$r \frac{\partial F_0}{\partial r}(x_{ft}) = \frac{x - x_{ft}}{\sqrt{(x-x_{ft})^2 + \beta^2 r^2}} \xrightarrow[x \to x_{fl}]{} -1 \tag{B.3}$$

$$r \frac{\partial F_0}{\partial r}(x_{fl}) = \frac{x - x_{fl}}{\sqrt{(x-x_{fl})^2 + \beta^2 r^2}} = \frac{1}{\sqrt{1 + \beta^2 \left(\frac{r}{x-x_{fl}}\right)^2}}$$

$$\xrightarrow[x \to x_{fl}]{r \to R(x)} \frac{1}{\sqrt{1 + \beta^2 \left(\frac{dR}{dx}\right)^2}} = g_1 \tag{B.4}$$

$$r \frac{\partial F_0}{\partial r}(\xi) = \frac{x - \xi}{\sqrt{(x-\xi)^2 + \beta^2 r^2}} \xrightarrow[x \to x_{fl}]{} -1 \tag{B.5}$$

It follows that

$$-\frac{1}{4\pi}\left\{-f_0(x_{ft})-f_0(x_{fl})g_1+\int_{x_{fl}}^{x_{ft}} f_0'(\xi)d\xi\right\}$$
$$=\frac{1}{4\pi}f_0(x_{fl})(1+g_1)=\cos\alpha\left.\frac{dR}{dx}\right|_{x=x_{fl}} \tag{B.6}$$

Therefore,

$$f_0(x_{fl})=\frac{4\pi\cos\alpha\, R\left.\frac{dR}{dx}\right|_{x=x_{fl}}}{1+g_1} \tag{B.7}$$

(2) $f_1(x_{fl})$

The first-order Fourier component of Eq. (5) is

$$\frac{\partial\phi_f^{(1)}}{\partial r}+\frac{\partial\phi_w^{(1)}}{\partial r}=-\sin\alpha \tag{B.8}$$

Again, Eq. (6) gives

$$-\frac{1}{4\pi}\left\{f_1(x_{ft})r^2\frac{\partial F_1}{\partial r}(x_{ft})-f_1(x_{fl})\,r^2\frac{\partial F_1}{\partial r}(x_{fl})-\int_{x_{fl}}^{x_{ft}} r^2\frac{\partial F_1}{\partial r}(\xi)\,f_1'(\xi)d\xi\right\}_{r=R(x)}$$
$$+r^2\left.\frac{\partial\phi_w^{(1)}}{\partial r}\right|_{r=R(x)}=-R^2\sin\alpha \tag{B.9}$$

To find $f_1(x_{fl})$, Eq. (B.9) will be differentiated once with x before the limiting values as $x\to x_{fl}$ are evaluated. Hence,

$$\frac{\partial}{\partial x}\left[r^2\frac{\partial F_1}{\partial r}(x_{ft})\right]=1+\frac{x-x_{ft}}{\sqrt{(x-x_{ft})^2+\beta^2r^2}}+(x-x_{ft})\left\{\frac{1}{\sqrt{(x-x_{ft})^2+\beta^2r^2}}\right.$$
$$\left.-\frac{(x-x_{ft})\left[(x-x_{ft})+\beta^2r\frac{dr}{dx}\right]}{\left[(x-x_{ft})^2+\beta^2r^2\right]^{3/2}}\right\}$$
$$\xrightarrow[x\to x_{fl}]{r\to R(x)} 1-1+\{-1+1\}=0 \tag{B.10}$$

where $\beta^2 r \frac{dr}{dx}$ is assumed small compared with $(x - x_{fl})$ as $x \to x_{fl}$.

$$\frac{\partial}{\partial x}\left[r^2 \frac{\partial F_1}{\partial r}(x_{fl})\right] = 1 + \frac{x - x_{fl}}{\sqrt{(x-x_{fl})^2 + \beta^2 r^2}} + (x - x_{fl})\left\{ \frac{1}{\sqrt{(x-x_{fl})^2 + \beta^2 r^2}} - \frac{(x-x_{fl})\left[x - x_{fl} + \beta^2 r \frac{dr}{dx} \right]}{\left[(x-x_{fl})^2 + \beta^2 r^2\right]^{3/2}} \right\}$$

$$\xrightarrow[x \to x_{fl}]{r \to R(x)} 1 + g_1 + \left\{ g_1 - \frac{1 + \beta^2 \left(\frac{dr}{dx}\right)^2}{\left[1 + \beta^2 \left(\frac{dr}{dx}\right)^2\right]^{3/2}} \right\} = 1 + g_1 \tag{B.11}$$

Similar to Eq. (B.10), it can be shown that

$$\frac{\partial}{\partial x}\left[r^2 \frac{\partial F_1}{\partial r}(\xi)\right] \longrightarrow 0 \tag{B.12}$$

It follows that

$$-\frac{1}{4\pi}\left\{ -f_1(x_{fl})(1+g_1) \right\} + 2R \frac{dR}{dx}\Big|_{x = x_{fl}} \sum_m N^{(1)}_{fw_m} \gamma_{w_m} \Big|_{x = x_{fl}}$$

$$= -2R \frac{dR}{dx}\Big|_{x = x_{fl}} \sin\alpha$$

$$f_1(x_{fl}) = -\frac{8\pi R \frac{dR}{dx}\Big|_{x = x_{fl}}}{1 + g_1} \left[\sin\alpha + \sum_m N^{(1)}_{fw_m} \gamma_{w_m} \Big|_{x = x_{fl}} \right] \tag{B.13}$$

By inspection, it can be determined that with jet on, Eq. (B.13) will be modified to be

$$f_1(x_{fl}) = -\frac{8\pi R \frac{dR}{dx}\Big|_{x = x_{fl}}}{1 + g_1} \left\{ \sum N^{(1)}_{fw} \gamma_{wa} + \sum N^{(1)}_{fJ} \gamma_{oj} \right\}_{x = x_{fl}} \tag{B.14}$$

due to the additional flow singularities γ_{wa} and γ_{oj} because of jet interaction.

Similar procedure can also be followed to derive the expressions for $f_n(x_{fl})$, $n \geq 2$. However, the algebra will be more complicated. On the other hand, by observing Eq. (B.13) it can be determined that $f_n(x_{fl})$, $n \geq 2$, would depend on the higher Fourier components of the wing or jet induced velocities at the pointed nose. Clearly, these higher Fourier components are zero. Hence,

$$f_n(x_{fl}) = 0 \quad , \quad n \geq 2 \tag{B.15}$$

Eq. (B.15) can be easily shown by the slender body theory.

It should be noted that $f_n(x_{fl})$ will affect mainly the pressure distribution near the nose of the fuselage. Because its effect is small on the over-all characteristics, it will be assumed zero in the prediction of lateral-directional stability derivatives.

Appendix C

Calculation of Fuselage Aerodynamic Characteristics

(1.) Calculation of the u-perturbed velocity on the fuselage surface due to the vortex multiplets.

As will be shown later in this Appendix, the sectional normal force coefficient C_N is to be computed at the integration stations (i.e., at the stations where $f'(\xi)$-values have been computed). Therefore, C_p and u are also to be computed at the same stations. For better accuracy, $u=\frac{\partial \phi_f}{\partial x}$ will be computed as follows.

Differentiating Eq. (2) for the fuselage velocity potential with x, it is obtained that

$$\frac{\partial \phi_f}{\partial x} = -\frac{1}{4\pi} \sum_n \begin{pmatrix} \cos n\theta \\ \sin n\theta \end{pmatrix} \left\{ f_n(x_{ft}) \frac{\partial F_n}{\partial x}(x_{ft}) - f_n(x_{fl}) \frac{\partial F_n}{\partial x}(x_{fl}) - \int_{x_{fl}}^{x_{ft}} \frac{\partial F_n}{\partial x}(\xi) f_n'(\xi) d\xi \right\} \tag{C.1}$$

The integral will be integrated in the following way. Consider $n=0$. Then

$$\frac{\partial F_o}{\partial x}(\xi) = -\frac{1}{\sqrt{(x-\xi)^2+\beta^2 r^2}} \tag{C.2}$$

$$\int_{x_{fl}}^{x_{ft}} -\frac{1}{\sqrt{(x-\xi)^2+\beta^2 r^2}} f_o'(\xi) d\xi = -\int_{x_{fl}}^{x_{ft}} \frac{f_o'(\xi)-f_o'(x)}{\sqrt{(x-\xi)^2+\beta^2 r^2}} d\xi - f_o'(x) \int_{x_{fl}}^{x_{ft}} \frac{d\xi}{\sqrt{(x-\xi)^2+\beta^2 r^2}}$$

$$\cong -\frac{l}{2} \frac{\pi}{N_F} \sum_k \frac{[f_{ok}' - f_o'(x)]}{\sqrt{(x-\xi_k)^2+\beta^2 r^2}} \sin\theta_{ik} + f_o'(x) \ell_n \frac{x-x_{ft}+\sqrt{(x-x_{ft})^2+\beta^2 r^2}}{x-x_{fl}+\sqrt{(x-x_{fl})^2+\beta^2 r^2}} \tag{C.3}$$

It follows that

$$\frac{\partial \phi_f^{(0)}}{\partial x} = -\frac{1}{4\pi}\left\{ f_0(x_{ft}) \frac{\partial F_0}{\partial x}(x_{ft}) - f_0(x_{fl}) \frac{\partial F_0}{\partial x}(x_{fl}) + \frac{\ell}{2} \frac{\pi}{N_F} \sum_k \frac{f_{0k}' - f_0'(x)}{\sqrt{(x-\xi_k)^2+\beta^2 r^2}} \cdot \right.$$

$$\left. \cdot \sin\theta_{fk} - f_0'(x) \ell_n \frac{x - x_{ft} + \sqrt{(x-x_{ft})^2+\beta^2 r^2}}{x - x_{fl} + \sqrt{(x-x_{fl})^2+\beta^2 r^2}} \right\} \qquad (C.4)$$

Note that x is the location where $\frac{\partial \phi_f}{\partial x}$ is to be computed and in the present case coincides with ξ_k .

Similarly, for different n , it can be shown that

$$\frac{\partial \phi_f^{(n)}}{\partial x} = -\frac{1}{4\pi} \begin{pmatrix} \cos n\theta \\ \sin n\theta \end{pmatrix} \left\{ f_n(x_{ft}) \frac{\partial F_n}{\partial x}(x_{ft}) - f_n(x_{fl}) \frac{\partial F_n}{\partial x}(x_{fl}) \right.$$

$$\left. - \int_{x_{fl}}^{x_{ft}} \frac{\partial F_n}{\partial x}(\xi) \left[f_n'(\xi) - f_n'(x) \right] d\xi - f_n'(x) \int_{x_{fl}}^{x_{ft}} \frac{\partial F_n}{\partial x}(\xi) d\xi \right\} \qquad (C.5)$$

where

$$\int_{x_{fl}}^{x_{ft}} \frac{\partial F_n}{\partial x}(\xi) \left[f_n'(\xi) - f_n'(x) \right] d\xi \cong \frac{\ell}{2} \frac{\pi}{N_F} \sum_k \frac{\partial F_n}{\partial x}(\xi_k) \left[f_n'(\xi_k) - f_n'(x) \right] \sin\theta_{fk} \qquad (C.6)$$

$$\frac{\partial F_n}{\partial x}(\xi) = -\frac{1}{r^n} \frac{\left[x - \xi + \sqrt{(x-\xi)^2+\beta^2 r^2} \right]^n}{\sqrt{(x-\xi)^2+\beta^2 r^2}} \qquad (C.7)$$

$$\int_{x_{fl}}^{x_{ft}} \frac{\partial F_n}{\partial x}(\xi) d\xi = \frac{1}{n} \frac{\left[x - \xi + \sqrt{(x-\xi)^2+\beta^2 r^2} \right]^n}{r^n} \Bigg|_{x_{fl}}^{x_{ft}} \qquad (C.8)$$

(2.) Fuselage normal force and moment coefficients

Once the pressure distribution on the fuselage surface is computed, it can be integrated to give the sectional normal force coefficient $C_{N(f)}$. Integrating C_N along the fuselage axis will produce the total normal force coefficient. According to Eq. (48), it is given by

$$C_{N(f)} = \frac{x_{ft} - x_{fl}}{2 S_w} \int_0^{\phi_p} r\, C_{N(f)} \sin\phi \, d\phi \tag{C.9}$$

Let

$$f(\phi) = \frac{x_{ft} - x_{fl}}{2 S_w} r\, C_{N(f)} \sin\phi \tag{C.10}$$

$f(\phi)$ can be developed in a cosine Fourier series:

$$f(\phi) = a_0 + \sum_1^{N_F} a_j \cos j\phi \tag{C.11}$$

where

$$a_0 = \frac{1}{\pi}\int_0^{\pi} f(\phi)\, d\phi \cong \frac{1}{\pi}\frac{\pi}{N_F}\sum_{k=1}^{N_F} f(\phi_k) \tag{C.12}$$

$$a_j = \frac{2}{\pi}\int_0^{\pi} f(\phi)\cos j\phi \, d\phi \cong \frac{2}{\pi}\frac{\pi}{N_F}\sum_{k=1}^{N_F} f(\phi_k)\cos j\phi_k \tag{C.13}$$

$$\phi_k = \frac{2k-1}{2N_F}\pi \tag{C.14}$$

Once the Fourier coefficients are obtained, direct integration of the series will give $C_{N(f)}$:

$$C_{N(f)} = \int_0^{\phi_p} f(\phi)\, d\phi = a_0 \phi_p + \sum_1^{N_F} \frac{a_j}{j} \sin j\phi_p \tag{C.15}$$

Similarly, the moment coefficient can be obtained as

$$C_{m(f)} = -\frac{x_{ft} - x_{fl}}{2 S_w \bar{c}} \int_0^{\phi_p} r C_{N(f)} x \sin\phi \, d\phi$$

$$= -\frac{1}{\bar{c}} \int_0^{\phi_p} f(\phi) x \, d\phi = -\frac{1}{\bar{c}} \int_0^{\phi_p} \left(a_0 + \sum_1^{N_F} a_j \cos j\phi\right)\left[x_{fl} + \frac{l}{2}(1-\cos\phi)\right] d\phi$$

$$= -\frac{x_{fl}}{\bar{c}} C_{N(f)} - \frac{l}{2\bar{c}}\left[a_0 \phi_p + \sum_1^{N_F} \frac{a_j}{j} \sin j\phi_p - a_0 \sin\phi_p - \frac{a_1}{2}\left(\phi_p + \frac{1}{2}\sin 2\phi_p\right)\right.$$

$$\left. - \sum_2^{N_F} \frac{a_j}{2}\left(\frac{\sin(j-1)\phi_p}{j-1} + \frac{\sin(j+1)\phi_p}{j+1}\right)\right] \qquad (C.16)$$

Appendix D

A Trigonometric Interpolation Formula for the Calculation of Streamwise Vortex Density

As shown in Eq. (65), the streamwise vortex density γ_x can be computed if $\frac{\partial \Gamma}{\partial y'}$ is known on the wing surface, where y' is the inclined distance as shown in Fig. D.1. Assume that

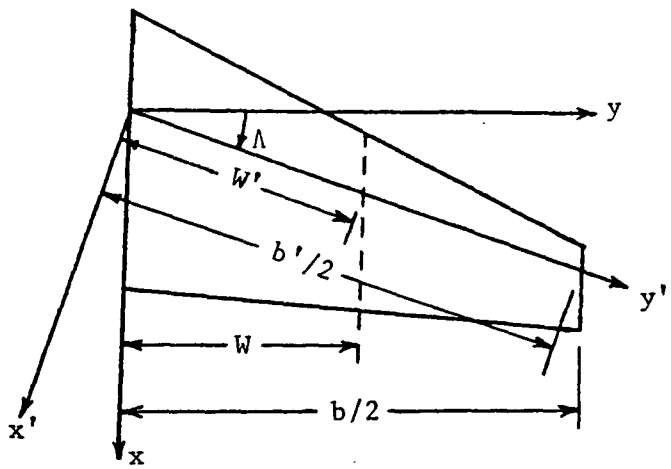

Figure D.1 Geometry Definition

the Γ -values defined in the section of width W are to be used for interpolation to find $\frac{\partial \Gamma}{\partial y'}$. The following two transformations will be used:

$$y = -\frac{b}{2}\cos\phi \tag{D.1}$$

$$y' = \frac{W'}{2}(1-\cos\theta) + y'_0 \tag{D.2}$$

Eq. (D.1) transforms the interval $y=(-\frac{b}{2}, \frac{b}{2})$ into $\phi=(0,\pi)$ and Eq. (D.2) transforms the inclined interval $y'=(y'_0, y'_0+W')$ into $\theta=(0,\pi)$.

Since it is well known that Γ possesses square-root singularities at both tips, it is numerically more accurate to develop $\Gamma \sin\phi$, instead of Γ itself, into a cosine Fourier series.

Let

$$g(\theta) = \Gamma \sin\phi \tag{D.3}$$

and

$$g(\theta) = a_0 + \sum_{j=1}^{M} a_j \cos j\theta \tag{D.4}$$

where the Fourier coefficients are given by

$$a_0 = \frac{1}{\pi}\int_0^{\pi} g(\theta)\,d\theta \cong \frac{1}{M}\left[\frac{1}{2}(g_0 + g_M) + \sum_{k=1}^{M-1} g_k\right] \tag{D.5}$$

$$a_j = \frac{2}{\pi}\int_0^{\pi} g(\theta)\cos j\theta\,d\theta \cong \frac{2}{M}\left[\frac{1}{2}(g_0 + g_M\cos j\theta_M) + \sum_{k=1}^{M-1} g_k \cos j\theta_k\right] \tag{D.6}$$

where the conventional, not midpoint, trapezoidal rule has been used because the Γ-values are computed at the locations which are not appropriate for the midpoint rule. θ_k is defined as

$$\theta_k = \frac{k\pi}{M} \tag{D.7}$$

If Eqs. (D.5) and (D.6) are substituted into Eq. (D.4), it is obtained that

$$\begin{aligned} g(\theta) = a_0 &+ \frac{2}{M}\sum_{j=1}^{M}\sum_{k=1}^{M-1} g_k \cos j\theta_k \cos j\theta \\ &+ \frac{1}{M}\sum_{j=1}^{M}(g_0 + g_M\cos j\theta_M)\cos j\theta \end{aligned} \tag{D.8}$$

Differentiation of $g(\theta)$ with respect to θ gives

$$\begin{aligned} \frac{dg}{d\theta} = &-\frac{2}{M}\sum_{j=1}^{M}\sum_{k=1}^{M-1} g_k\, j \cos j\theta_k \sin j\theta \\ &- \frac{1}{M}\sum_{j=1}^{M}(g_0 + g_M\cos j\theta_M)\, j \sin j\theta \end{aligned} \tag{D.9}$$

Eq. (D.9) is to be evaluated at θ_i , where

$$\theta_i = \frac{i\pi}{M} \tag{D.10}$$

Using known trigonometric relations, Eq. (D.9) becomes

$$\frac{dq}{d\theta_i} = -\frac{1}{M}\sum_{k=1}^{M-1} g_k \sum_{j=1}^{M} j\left[\sin j(\theta_k+\theta_i) - \sin j(\theta_k-\theta_i)\right]$$
$$- \frac{1}{M} g_0 \sum_{j=1}^{M} j \sin j\theta_i - \frac{1}{M}\frac{g_N}{2}\sum_{j=1}^{M} j\left[\sin j(\theta_M+\theta_i) - \sin j(\theta_M-\theta_i)\right] \tag{D.11}$$

However, it is known that (Ref. 21)

$$\sum_{j=1}^{M} j \sin jx = \frac{M\sin(M+1)x - (M+1)\sin Mx}{2(\cos x - 1)} \tag{D.12}$$

Hence,

$$\sum_{j=1}^{M} j\left[\sin j(\theta_k+\theta_i) - \sin j(\theta_k-\theta_i)\right]$$
$$= \frac{M(-1)^{k+i}}{2}\left[\frac{\sin(\theta_k+\theta_i)}{\cos(\theta_k+\theta_i)-1} - \frac{\sin(\theta_k-\theta_i)}{\cos(\theta_k-\theta_i)-1}\right]$$
$$= \frac{M(-1)^{k+i}}{2}\left[-\frac{\cos\left(\frac{\theta_k+\theta_i}{2}\right)}{\sin\left(\frac{\theta_k+\theta_i}{2}\right)} + \frac{\cos\left(\frac{\theta_k-\theta_i}{2}\right)}{\sin\left(\frac{\theta_k-\theta_i}{2}\right)}\right]$$
$$= -M(-1)^{k+i}\frac{\sin\theta_i}{\cos\theta_k - \cos\theta_i} \qquad , k \neq i \tag{D.13}$$

Similarly, it can be shown that

$$\sum_{j=1}^{M} j \sin j\theta_i = \frac{M\sin(M+1)\theta_i - (M+1)\sin M\theta_i}{2(\cos\theta_i - 1)}$$
$$= -\frac{M(-1)^i \sin\theta_i}{2(1-\cos\theta_i)} \tag{D.14}$$

$$\sum_{j=1}^{M} j\left[\sin j(\theta_M+\theta_i)-\sin j(\theta_M-\theta_i)\right]$$

$$= \frac{M(-1)^{M+i}}{2}\left[\frac{\sin(\theta_M+\theta_i)}{\cos(\theta_M+\theta_i)-1}-\frac{\sin(\theta_M-\theta_i)}{\cos(\theta_M-\theta_i)-1}\right]$$

$$= M(-1)^{M+i}\frac{\sin\theta_i}{1+\cos\theta_i} \qquad \text{(D.15)}$$

If k=i, Eq. (D.13) will be revised to be

$$\sum_{j=1}^{M} j\sin 2j\theta_i = \frac{M\sin(M+1)2\theta_i}{2(\cos 2\theta_i-1)} = -\frac{M\sin 2\theta_i}{2(1-\cos 2\theta_i)}$$

$$= -\frac{M}{2}\frac{\cos\theta_i}{\sin\theta_i} \qquad \text{(D.16)}$$

Therefore, Eq. (D.11) becomes

$$\frac{dg}{d\theta_i} = \sum_{k=1}^{M-1}{}' g_k(-1)^{k+i}\frac{\sin\theta_i}{\cos\theta_k-\cos\theta_i}+\frac{1}{2}g_i\frac{\cos\theta_i}{\sin\theta_i}$$

$$+\frac{1}{2}g_0\frac{(-1)^i\sin\theta_i}{1-\cos\theta_i}-\frac{1}{2}g_M(-1)^{M+i}\frac{\sin\theta_i}{1+\cos\theta_i} \qquad \text{(D.17)}$$

where the prime on the summation sign implies that the term with $k=i$ is to be omitted.

Differentiating Eq. (D.3) with y' gives

$$\frac{\partial g}{\partial y'} = \frac{dg}{d\theta}\frac{\partial\theta}{\partial y'} = \frac{\partial\Gamma}{\partial y'}\sin\phi+\Gamma\cos\phi\frac{\partial\phi}{\partial y'} \qquad \text{(D.18)}$$

Solving for $\frac{\partial\Gamma}{\partial y'}$, it is obtained that

$$\frac{\partial \Gamma}{\partial y'_i} = \frac{1}{\sin\phi_i}\left\{\frac{dg}{d\theta_i}\frac{d\theta_i}{dy'} - \Gamma\cos\phi_i\frac{d\phi}{dy}\cos\Lambda\right\}$$

$$= \frac{1}{\sin\phi_i}\left\{\frac{dg}{d\theta_i}\frac{2}{W'\sin\theta_i} - \frac{\Gamma\cos\phi_i}{\frac{b}{2}\sin\phi_i}\cos\Lambda\right\} \qquad \text{(D.19)}$$

Eqs. (D.17) and (D.19) represent the desired formula for computing $\frac{\partial \Gamma}{\partial y'}$.

It should be noted that g_0 and g_M can be obtained by interpolation.

Appendix E

Calculation of Tip Suction

According to Eq. (66), the tip suction per unit length of the tip chord is given by

$$S_t(x) = \pi\rho\, G^2(x) \tag{E.1}$$

where $G(x)$ is related to the circulation through the following relation (Ref. 18)

$$G(x) = \sqrt{\frac{b}{2}} \lim_{y \to \frac{b}{2}} \sqrt{1 - \left(\frac{y}{b/2}\right)}\ \frac{1}{2}\frac{\partial \Gamma}{\partial y} \tag{E.2}$$

Near the right tip, Eq. (E.2) implies that

$$\Gamma(x, y) \cong -4G(x)\sqrt{\frac{b}{2}}\sqrt{1 - \left(\frac{y}{\frac{b}{2}}\right)} \tag{E.3}$$

Eq. (D.19) shows that

$$\sin\phi\ \frac{\partial \Gamma}{\partial y'} = \frac{dg}{d\theta}\ \frac{2}{W'\sin\theta} - \frac{\Gamma\cos\phi}{\frac{b}{2}\sin\phi}\cos\Lambda \tag{E.4}$$

But at the tip,

$$\frac{\partial \Gamma}{\partial y'} = \frac{\partial \Gamma}{\partial x}\frac{\partial x}{\partial y'} + \frac{\partial \Gamma}{\partial y}\frac{\partial y}{\partial y'} = \frac{\partial \Gamma}{\partial y}\cos\Lambda \tag{E.5}$$

because $\frac{\partial \Gamma}{\partial x} = -\gamma_y$ vanishes at the tip. Hence, the objective is to find the limiting value of the following equation:

$$\lim_{y \to \frac{b}{2}} \left\{ \sin\phi\ \frac{\partial \Gamma}{\partial y} = \frac{dg}{d\theta}\ \frac{2}{W\sin\theta} - \frac{\Gamma\cos\phi}{\frac{b}{2}\sin\phi} \right\} \tag{E.6}$$

where $W = W'\cos\Lambda$ has been used. Differentiating Eq. (E.3) with respect to y gives

$$\frac{\partial \Gamma}{\partial y} = \frac{2G}{\sqrt{\frac{b}{2}}}\ \frac{1}{\sqrt{1 - \left(\frac{y}{b/2}\right)}} \tag{E.7}$$

It follows that

$$\lim_{y\to\frac{b}{2}} \sin\phi \frac{\partial \Gamma}{\partial y} = \lim_{y\to\frac{b}{2}} \sqrt{1+\left(\frac{y}{b/2}\right)} \frac{2G}{\sqrt{\frac{b}{2}}} = 2\sqrt{2}\frac{G}{\sqrt{\frac{b}{2}}} \tag{E.8}$$

$$\lim_{y\to\frac{b}{2}} \frac{\Gamma\cos\phi}{\frac{b}{2}\sin\phi} = \lim_{y\to\frac{b}{2}} \frac{-4G\sqrt{\frac{b}{2}}\sqrt{1-\left(\frac{y}{b/2}\right)}(-1)}{\frac{b}{2}\sqrt{1-\left(\frac{y}{b/2}\right)^2}} = \frac{2\sqrt{2}\,G}{\sqrt{\frac{b}{2}}} \tag{E.9}$$

where $\sin\phi = \sqrt{1-\left(\frac{y}{b/2}\right)^2}$ (see Eq. (D.1)). Furthermore, Eq. (D.17) gives

$$\frac{dg}{d\theta_i}\frac{2}{W\sin\theta_i} = \frac{2}{W}\sum_{k=1}^{M-1}\Gamma_k \sin\phi_k \frac{(-1)^{k+i}}{\cos\theta_k - \cos\theta_i} + \frac{1}{W}\Gamma_0 \sin\phi_0 \frac{(-1)^i}{1-\cos\theta_i}$$
$$- \frac{1}{W}\Gamma_M \sin\phi_M \frac{(-1)^{M+i}}{1+\cos\theta_i} \tag{E.10}$$

where the second term on the right hand side of Eq. (D.17) has been combined into the first term because i will not be equal to k in the present case. Note that at the tip $i = M$ and $\theta_i = \pi$ (see Eq. (D.10)). In addition,

$$\cos\theta = 1 - \frac{2}{W}(y - y_0) \tag{E.11}$$

$$1+\cos\theta_M = \lim_{y\to\frac{b}{2}} 2\left(1 - \frac{y-y_0}{W}\right) \tag{E.12}$$

where Eq. (E.11) is obtained by multiplying Eq. (D.2) by $\cos\Lambda$. The last term in Eq. (E.10) has the following limiting value as $y\to\frac{b}{2}$:

$$\lim_{\substack{y\to\frac{b}{2}\\ i\to M}} \frac{\Gamma_i \sin\phi_i}{1+\cos\theta_i} = \lim_{y\to\frac{b}{2}} \frac{-4G\sqrt{\frac{b}{2}}\sqrt{1-\left(\frac{y}{b/2}\right)}\sqrt{1-\left(\frac{y}{b/2}\right)^2}}{2\left(1-\frac{y-y_0}{W}\right)}$$
$$= \lim_{y\to\frac{b}{2}} \frac{-4G\sqrt{\frac{b}{2}}\left[1-\left(\frac{y}{b/2}\right)\right]\sqrt{1+\left(\frac{y}{b/2}\right)}}{2\left(1-\frac{y-y_0}{W}\right)}$$
$$= -2G\sqrt{\frac{b}{2}}\sqrt{2}\frac{-1/b/2}{-\frac{1}{W}} = -2\sqrt{2}\,G\frac{W}{\sqrt{\frac{b}{2}}} \tag{E.13}$$

where the third step was obtained by applying L'Hopital's rule.

Eq. (E.10) now becomes

$$\lim_{\substack{y\to\frac{b}{2}\\ i\to M}} \frac{d\mathcal{G}}{d\theta_i}\frac{2}{W\sin\theta_i} = \frac{2}{W}\sum_{k=1}^{M-1}\Gamma_k \sin\phi_k \frac{(-1)^{k+M}}{\cos\theta_k+1} + \frac{1}{W}\Gamma_o\sin\phi_o\frac{(-1)^M}{2} + \frac{2\sqrt{2}\,G}{\sqrt{\frac{b}{2}}} \tag{E.14}$$

Substituting Eqs. (E.8), (E.9) and (E.14) into Eq. (E.6) gives

$$2\sqrt{2}\,\frac{G}{\sqrt{\frac{b}{2}}} = \frac{2}{W}\sum_{k=1}^{M-1}\Gamma_k\sin\phi_k\frac{(-1)^{k+M}}{1+\cos\theta_k} + \frac{1}{W}\Gamma_o\sin\phi_o\frac{(-1)^M}{2} \tag{E.15}$$

From Eq. (E.15), $G(x)$ can be determined.

The local tip suction coefficient is defined as

$$C_{\ell,tip} = \frac{S_\ell(x)}{\frac{1}{2}\rho V_\infty^2 c_x} = \frac{2\pi G^2}{c_x}\,,\quad V_\infty = 1 \tag{E.16}$$

The total tip suction force is found from

$$F_\ell = 2\int_{x_{\ell,t}}^{x_{t,t}} \pi\rho G^2 dx = c_x\int_0^\pi \pi\rho G^2\sin\theta\, d\theta$$

$$\cong c_x\pi\rho\frac{\pi}{N}\sum_{k=1}^{N} G_k^2\sin\theta_k \tag{E.17}$$

It follows that the tip suction coefficient is

$$C_{\ell,tip} = \frac{F_\ell}{\frac{1}{2}\rho V_\infty^2 S_w} = \frac{2c_\ell}{S_w}\frac{\pi^2}{N}\sum_{k=1}^{N} G_k^2\sin\theta_k \tag{E.18}$$

Eq. (E.18) can be used to estimate the side edge contribution to the vortex lift as shown in Ref. 18.